BEN-GURION UNIVERSITY OF THE NEGEV

THE FACULTY OF NATURAL SCIENCES

DEPARTMENT OF GEOLOGICAL & ENVIRONMENTAL SCIENCES

NUMERICAL SIMULATION OF BLOCK DISPLACEMENT DUE TO TEMPERATURE FLUCTUATIONS

THESIS SUBMITTED IN PARTIAL FULFILLMENT OF THE REQUIREMENTS FOR THE MASTER OF SCIENCES DEGREE

BY: YUVAL KEISSAR

UNDER THE SUPERVISION OF:

PROF. YOSSEF H. HATZOR

DR. DAGAN BAKUN-MAZOR

MARCH 2018

BEN-GURION UNIVERSITY OF THE NEGEV

THE FACULTY OF NATURAL SCIENCES

DEPARTMENT OF GEOLOGICAL & ENVIRONMENTAL SCIENCES

NUMERICAL SIMULATION OF BLOCK DISPLACEMENT DUE TO TEMPERATURE FLUCTUATIONS

THESIS SUBMITTED IN PARTIAL FULFILLMENT OF THE REQUIREMENTS FOR THE MASTER OF SCIENCES DEGREE

BY: YUVAL KEISSAR

UNDER THE SUPERVISION OF:

PROF. YOSSEF H. HATZOR

DR. DAGAN BAKUN-MAZOR

Signature of student: _____ Date: _____

Signature of supervisor: _____ Date: ___4.3.2018___

Signature of supervisor: _____ Date: ___4.3.2018___

Signature of chairperson of the committee for graduate studies: _____

Date: _____

MARCH 2018

Abstract

In this research, a thermally induced wedging-ratcheting mechanism for slope stability is investigated using a three-dimensional version of the numerical Distinct Element Method (3DEC). Our goal is to examine whether daily or annual surface temperature fluctuations can induce downslope, irreversible displacement and to create a quantitative model for thermally controlled block displacements. Problems of heat conduction are often too complex to solve using analytical solutions alone. Numerical approaches allow us to study complicated geomechanical problems for which exact analytical solutions do not exist or cannot be obtained. We construct a three-dimensional model in 3DEC to simulate the thermal expansion of a sliding block and the resulting block displacement down an inclined frictional slope. According to the proposed wedging-ratcheting mechanism, this displacement is assumed irreversible. Our results show that block displacement down the slope indeed occurs when the block boundaries are subjected to increased temperatures. Results of the numerical model are compared with a semi-analytical approach proposed by Pasten (2013) for the plastic displacement obtained in a single climatic cycle, and with experimental results obtained from a physical model in a climatically controlled room (Feldheim, 2017).

We compare numerical simulations with monitored displacements of a slender block in the East slope of Mount Masada as up until recently the governing mechanism for this block displacement has been assumed to be seismically driven. By application of our numerical approach to the exact physical dimensions of the block in the field we find that, in fact, thermal loading alone can explain the mapped accumulated displacement.

We believe this new, thermally-induced, failure mechanism may play a significant role in slope stability problems due to the cumulative and repetitive nature of the displacement, particularly in rock slopes in fractured rock masses that are exposed to high temperature oscillations.

Acknowledgements

I would like to thank Professor Yossi Hatzor for his guidance throughout this research. His mentorship was invaluable. I am fortunate to have learned from him about research and science.

I also wish to thank Dr. Dagan Bakun-Mazor for his guidance. He taught me a lot about how to conduct a scientific work. His input and attention to details improved this research a great deal.

I would like to express my gratitude to my friends and fellow graduate students for their support, fruitful discussions, and for the friendly coffee breaks: Doron Morad, Almog Baram, Omri Shitrit, Yair Gorodin, Nahum Kazaz, and Bengou He.

This research was funded by Israel Science Foundation through grant no. 1442/13. The support of Israel Science Foundation is thankfully acknowledged.

Finally, I thank my wife and partner, Zohar Eshed-Keissar, for all the support, understanding, and great care throughout these years.

Table of contents

List of figures

List of tables

Chapter 1 - Introduction

Slope instabilities may pose serious threats to humans and to property. Slope instabilities can develop both in rocks or soils. In order to predict, or even prevent this geotechnical hazard, we must study the underlying mechanisms that affect slope stability and cause slope failure.

In discontinuous rock masses, various environmentally controlled mechanisms can induce slope failure along pre-existing joints, such as seismic horizontal accelerations (e.g. Rodriguez et al., 1999), excessive pore water pressure (e.g. Iverson, 2000) and freeze-thaw of cleft water in joints (e.g. Matsuoka, 2008). Yet, many rock slope failures seem to be spontaneous, and cannot be explained by either of the mechanisms above.

There are other environmentally controlled mechanisms, thermally induced, that can affect slope stability. Thermal expansion and contraction of rocks close to the surface, due to seasonal warming and cooling, can change the state of stress at greater depths below the annual thermal active layer. Although stress changes are relatively small, they can cause slip on joints if the initial stress state is already close to failure (Gischig et al., 2011). Collins and Stock (2016) monitored an exfoliating granite cliff and found that heating of rock surface can cause outward expansion in an exfoliating rock, and further fracture propagation and consequent detachment or rock slabs. Gunzburger et al. (2005) demonstrated that cyclic surface temperature fluctuations might be a preparatory factor for failure, with day-to-day cumulative effect. The daily temperature fluctuations may cause irreversible displacement on joints. They simulated the mechanical response of a block on an inclined slope (Figure 1.1) to temperature oscillations using the numerical code UDEC (Itasca, 1996). The authors claim that due to thermal expansion and contraction solely, plastic conditions are achieved across the sliding plane, and the block gradually slides down the slope. They found that the irreversible and cumulative “crawling motion”, is of a magnitude of millimeters per cycle (Figure 1.2).

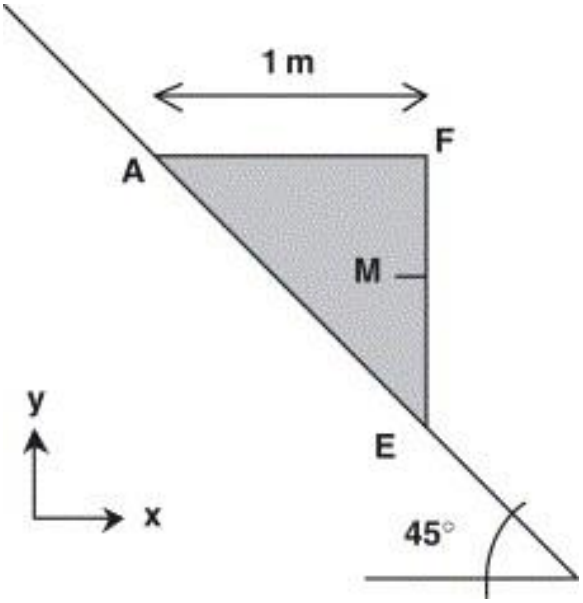

Figure 1.1 – Conceptual model for thermally induced block displacement. The block boundary EF was subjected to temperature oscillations and the displacement of point F was recorded during the simulation with UDEC (Gunzburger et al., 2005).

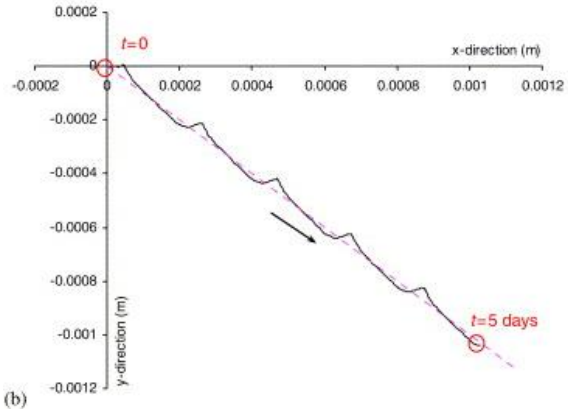

Figure 1.2 - Trajectory of point F during five cycles of heating and cooling (Gunzburger et al., 2005).

1.1. The proposed wedging-ratcheting mechanism

In previous work (Bakun-Mazor et al., 2013) the opening of joints in the rock slopes of Masada, Israel, was monitored for 2 years (Figure 1.3.) and a good correlation between surface temperature and joint opening was reported (Figure 1.4).

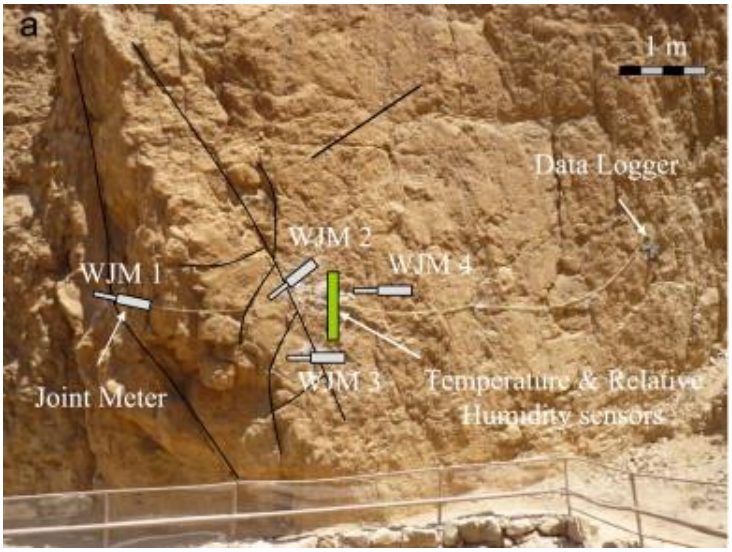

Figure 1.3 - Monitoring system at the west side of Masada

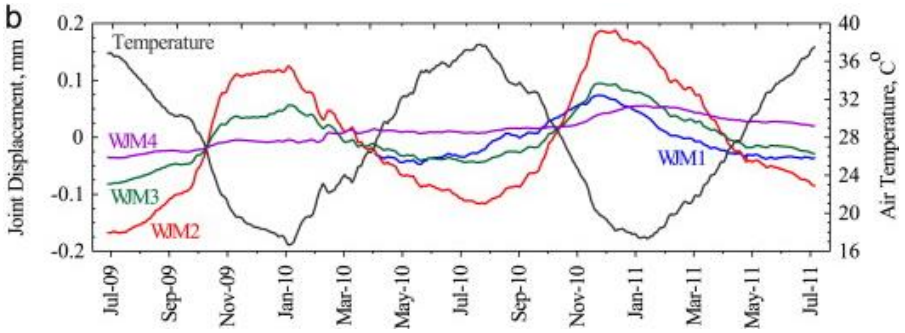

Figure 1.4 – Monitoring system output. Temperature and displacement vs. time (Bakun-Mazor et al., 2013)

These observations lead the researchers to introduce a new thermally induced mechanism, in which daily and seasonal temperature fluctuations can cause opening of a tension crack and block displacement along an inclined, pre-existing discontinuity. In this model, rock blocks from the neighboring surroundings are assumed to fall into an open pre-existing tension crack that separates between the rock mass and the sliding block, to form wedges that drive the mechanism forward, hence the wedging-ratcheting terminology (Figure 1.5).

Figure 1.5 - Wedge inside a tension crack, Wadi Arugot

When the temperature drops (during nighttime or winter season) the sliding block contracts, allowing the wedge to slide down the widening tension crack. When the temperature rises (during daytime or summer season), the sliding block expands, but the wedge is fixed in its previous place. In this state, compressive stresses develop around the wedge, pushing the sliding block down the slope. In the next cooling period, the sliding block contracts again, leading to opening of the tension crack, and further wedging down the tension crack, and the cycle completes with heating an expansion and sliding further down the slope. The proposed wedging-ratcheting mechanism is illustrated schematically in Figure 1.6.

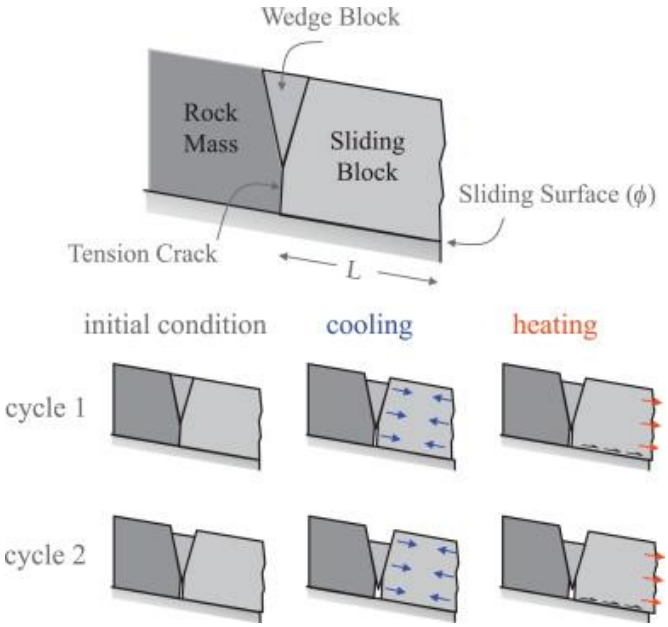

Figure 1.6 - Illustration of the wedging-ratcheting mechanism

An extensive research on the wedging-ratcheting mechanism was performed by Pasten & Santamarina (2013), who proposed a two-dimensional analytical solution to the problem, which is briefly reviewed here.

Assume the model presented in Figure 1.7. A sliding block of length L_B is resting on an inclined slope at an angle of η, separated from the rock mass (the left side of the model) with a wedge of length L_w.

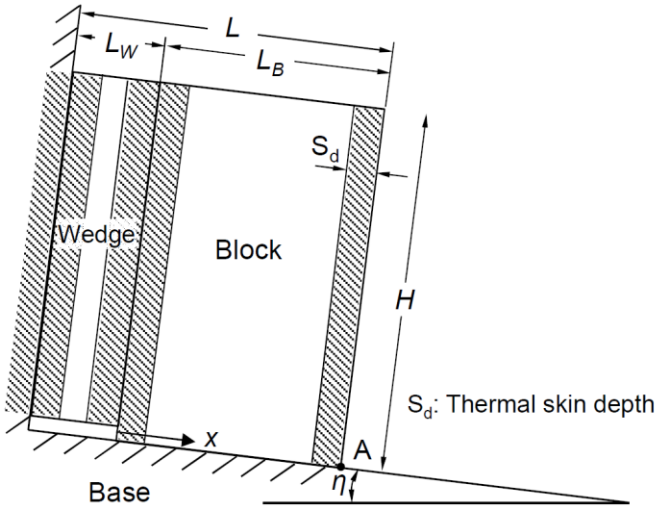

Figure 1.7 - Simplified block-wedge configuration (Pasten, 2013)

Under gravity only, the maximum force per unit width that the frictional strength of the sliding surface can sustain is:

$$F_{max} = H\gamma(L_B + \theta L_W)(\mu \cos\eta - \sin\eta) \quad (1)$$

Where:

$H =$ Block height [m].

$\gamma =$ Rock unit weight [N/m^3].

$\mu =$ Friction coefficient ($= \tan\phi$).

$\theta =$ A fraction of the wedge weight that is transferred to the sliding block (< 1).

When the system is subjected to temperature change, the sliding block expands. The magnitude of this expansion depends on the heat propagation front in the rock:

$$S_d = \begin{cases} \sqrt{0.5 \cdot D_T \cdot t_{exp}}\,, & t_{exp} < 0.5 \cdot L^2/D_T \\ L/2, & t_{exp} \geq 0.5 \cdot L^2/D_T \end{cases} \quad (2)$$

Where:

$S_d =$ Thermal skin depth [m].

$D_T =$ Thermal diffusivity, $= \frac{thermal\ conductivity}{density \cdot heat\ capacity}$ [m^2/s].

$L =$ Block length [m].

$t_{exp} =$ Exposure time [s].

The displacement of the toe of the sliding block (δ_T, m) depends on the thermal expansion of both the wedge and the sliding block itself:

$$\delta_T = \begin{cases} \alpha\Delta T(4 \cdot \beta \cdot S_d), & t_{exp} < 0.5 \cdot {L_W}^2/D_T < 0.5 \cdot {L_B}^2/D_T \\ \alpha\Delta T(L_W + 2 \cdot \beta \cdot S_d), & 0.5 \cdot {L_W}^2/D_T < t_{exp} < 0.5 \cdot {L_B}^2/D_T \\ \alpha\Delta T(L_W + \xi \cdot L_B + \beta \cdot S_d), & 0.5 \cdot {L_W}^2/D_T < 0.5 \cdot {L_B}^2/D_T < t_{exp} \end{cases} \quad (3)$$

Where α is the thermal expansion coefficient ($1/°C$) and ΔT is the temperature difference.

For short exposure time ($t_{exp} < 0.5 \cdot L^2/D_T$), the temperature distribution within the skin depth S_d is not uniform. The dimensionless coefficient $\beta \leq 1$ accounts for the non-uniform diffusive temperature distribution within the sliding block. For long exposure time ($0.5 \cdot L_W/D_T < 0.5 \cdot L_B/D_T < t_{exp}$) the temperature distribution within the blocks is uniform and the block expands to maximum. The dimensionless coefficient $\xi \leq 1$ accounts for the thermal expansion of the right portion of the block that does not contribute to constraining the system thermal expansion (Pasten, 2013).

As the block expands, thermal stress is accumulating on the interfaces between blocks. Thus, compressive stress is acting on the sliding block and it contracts elastically (δ_σ, m) by the following equation:

$$\delta_\sigma = \frac{F_{max}}{HE}\left(L_W + \frac{L_B}{2}\right) \tag{4}$$

Where F_{max} is described in eq. 1, and E is the Young's modulus of the rock (Pa). L_B is divided by 2 to account for the assumption that half of the sliding block towards the free surface is not contributing to the compressive stresses around the wedge.

The joint elastic displacement (δ_j, m) before any plastic displacement takes place is:

$$\delta_j = \frac{1}{k_j} \cdot \frac{F_{max}}{L_B} \tag{5}$$

Where k_j $[Pa/m]$ is the joint shear stiffness.

If $\delta_j = \delta_T - \delta_\sigma$ there will be no plastic displacement. Replacing in this equation the displacements described above (eqs. 3, 4, 5), the maximum temperature change required for imminent plastic displacement is:

$$\Delta T_{max} = \frac{F_{max}}{\alpha \cdot d(t_{exp}) \cdot E}\left[\frac{E}{k_j \cdot L_B} + \frac{L_W}{H} + \frac{L_B}{2H}\right] \tag{6}$$

Where $d(t_{exp})$ is the material length subjected to thermal expansion:

$$d(t_{exp}) = \begin{cases} 4 \cdot \beta \cdot S_d, & t_{exp} < 0.5 \cdot L_W/D_T < 0.5 \cdot L_B/D_T \\ L_W + 2 \cdot \beta \cdot S_d, & 0.5 \cdot L_W/D_T < t_{exp} < 0.5 \cdot L_B/D_T \\ L_W + \xi \cdot L_B + \beta \cdot S_d, & 0.5 \cdot L_W/D_T < 0.5 \cdot L_B/D_T < t_{exp} \end{cases} \quad (7)$$

If the external temperature exceeds ΔT_{max}, the sliding block will experience the following displacement:

$$\delta_j^p = \delta_T - \delta_\sigma - \delta_j \quad (8)$$

Later, Pasten has further developed the research, and validated the proposed analytical expressions experimentally and numerically (Pasten et al., 2015a). He examined the expected displacement and the failure mode for a range of geometric configurations, such as the shape of the wedge and the inclination of the slope (Pasten et al., 2015b). Greif et al. (2014) measured the displacement response of small sandstone samples to thermal fluctuations, in order to validate Pasten's equations for a range of block to wedge lengths ratios. The researchers also determined the threshold temperature change at which plastic deformation occurs, and their results are in agreement with the equations suggested by Pasten (2013).

Taboada et al. (2017) also studied the wedging-ratcheting mechanism. They monitored the displacement of a massive dolostone rock column, underlaid by weak layers of marl, and the temperature in the Larzac Plateau, Southern France, for 30 months. They showed that intra-seasonal short-term thermal cycles (ranging between 2-15 days) can cause thermally induced displacement of the column. The mechanism is similar to the wedging-ratcheting mechanism introduced by Bakun-Mazor et al. (2013), but Taboada et al. (2017) concluded that short-term temperature fluctuations are playing a more significant role than assumed previously. In Taboada's work, the displacement vector in each short-term thermal cycle is decomposed into two components: a reversible thermal displacement, associated with thermal expansion or contraction; and a plastic deformation at constant temperature, referred to as "thermo-mechanical creep". During autumn and winter seasons, short-term thermal cycles result in the most considerable plastic displacement

towards the free boundary. During spring, the plastic displacement is also towards the free boundary, but its magnitude is much smaller. During summer, the plastic deformation is negligible. The velocity of the rock, as obtained by Taboada et al. (2017) from field measurements, is ~1.2 mm per year.

1.2. Scope of research and objectives

In this study, the validity of the proposed wedging-ratcheting mechanism is examined using numerical simulations with the three-dimensional distinct element code 3DEC. The numerical results are compared with data obtained from lab experiments conducted by another member of BGU rock mechanics research group, of a physical model in a climatically controlled room.

The sensitivity of the model to geological and environmental variables such as duration of heating and cooling cycle, surface temperature amplitude, frictional properties of sliding interface, and thermal and mechanical properties of the host rocks are studied.

The final goal of this research is to create a theoretically based, numerically calibrated and experimentally validated quantitative model for thermally controlled block displacements. The predictive capabilities of the model are tested in the last part of the thesis using the rock slopes of Mt. Masada as a case study.

Chapter 2 - Research methods

To study realistic and complex heat transfer problems that apply to field cases, the solution must be expanded to two and preferably three dimensions. This can only be achieved by means of numerical approaches.

In this research, the proposed wedging-ratcheting mechanism is numerically simulated using the Distinct Element Method (DEM) code 3DEC (Itasca Consulting Group Inc., 2013a) developed by Cundall and colleagues (Cundall, 1988, Hart et al., 1988, Cundall and Hart, 1992). The theoretical foundation of this method is the formulation and solution of equations of motion of deformable blocks using explicit (using Finite Difference Method) time marching scheme (Jing, 2003). The code simulates the response of discontinuous medium to static, dynamic or thermal loading.

2.1. Mechanical implementations in 3DEC

The distinct element method is a way to numerically simulate the mechanical behavior of a rock mass (Cundall, 1988). The method has many other applications in rock and soil mechanics, structural analysis etc. (Jing, 2003). In this method, unlike continuum-based methods, the contacts between neighboring blocks are continuously changing with the deformation process.

2.1.1 Representation of blocks and contacts

Blocks in 3DEC are represented as convex polyhedra. Different blocks are formed by intersection of joints (or joint sets). Deformable blocks are further divided into a finite number of constant strain tetrahedra, which means that there is no stress or temperature gradient within a single zone. The tetrahedra have three translational degrees of freedom at each vertex (Cundall, 1988), to form a mesh of finite volume zones.

Contact detection is done using the principle of common plane (Cundall, 1988). The common plane bisects the space between two blocks (Figure 2.1). The code tests each block separately for contact with the common plane. There are six types of block contacts in 3DEC, contrived by the combination of vertex, edge and face. Using the principle of

common plane, a single vertex-to-plane test is adequate, provided the blocks are convex. Face and edge contacts are recognized by counting the number of vertex-to-plane contacts. The algorithm for locating and moving the common plane is based on geometry alone and is applied at every time step.

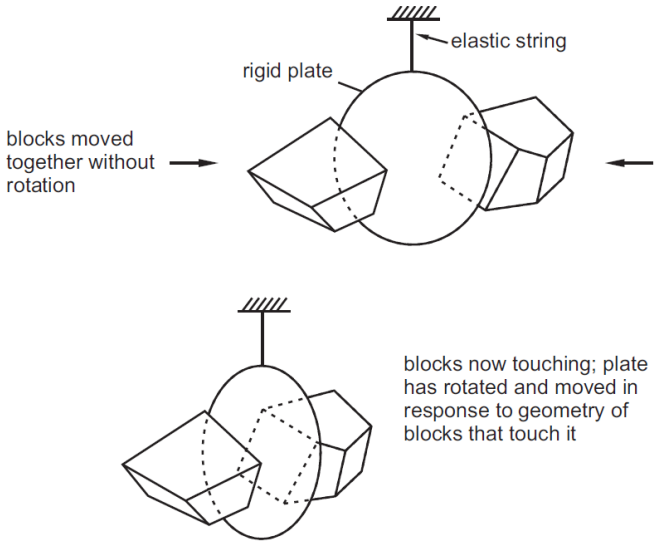

Figure 2.1 - Visualization for positioning of common plane in response to block geometry (Cundall, 1988)

Contacts between two neighboring blocks are characterized by normal and shear stiffness constants, represented by springs applied at the contacts in the normal and tangential directions, and by friction angle, represented by a spring-slip surface series (Figure 2.2).

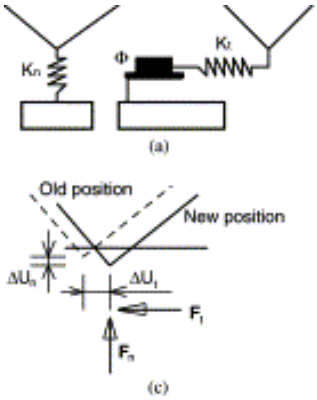

Figure 2.2 - Representation of contacts (Jing, 2003)

2.1.2 Equilibrium equations

Contact force update

As the deformation progresses, the contacts (or sub-contacts) must translate or rotate continuously. Therefore, the relative velocity across a sub-contact is calculated by the velocities of two opposing faces V and F ($V_i = V_i^V - V_i^F$). The velocity of tetrahedral vertex located on the face is calculated in eq. 16 (see below).

For deformable blocks, the velocities V_i^V, V_i^F are calculated by linear interpolation of the velocities of the vertices of the face:

$$V_i^F = W_a V_i^a + W_b V_i^b + W_c V_i^c \tag{9}$$

Where $W_{a,b,c}$ are weighting factors, which can be determined by transforming the coordinates of the three vertices of the face to a local coordinate system, which is co-planar to the face (e.g., the new coordinates of vertex a are X_a, Y_a):

$$W_a = \frac{Y^c X^b - Y^b X^c}{(x^a - X^c)(Y^b - Y^c) - (Y^a - Y^c)(X^b - X^c)} \tag{10}$$

The other weighting factors (W_b, W_c) can be calculated by circular permutation of the superscripts.

The increment displacement across a sub-contact with unit normal n_i is:

$$\Delta U_i = V_i \Delta t \tag{11}$$

The displacement can be further resolved to normal and shear components along the common plane (Figure 2.1):

$$\begin{aligned} \Delta U^n &= \Delta U_i n_i \\ \Delta U_i^s &= \Delta U_i - \Delta U_j n_i n_j \end{aligned} \tag{12}$$

Using the incremental sub-contacts displacement, the force increment can be calculated (taking compressive force as positive):

$$\begin{aligned} \Delta F^n &= -K_n \Delta U^n A_c \\ \Delta F_i^s &= -K_s \Delta U_i^s A_c \end{aligned} \tag{13}$$

Where K_n and K_s are the normal and shear stiffness of the joint, respectively and A_c is the sub-contact area.

The total normal and shear forces are updated for the contact:

$$F^n = F^n + \Delta F^n$$
$$F_i^s = F_i^s + \Delta F_i^s \quad (14)$$

Deformable block motion

If blocks cannot be assumed rigid (as for the case of thermal expansion studied here), fully deformable blocks permit internal deformation. During deformation process, the acceleration of each vertex in the tetrahedral zone (often referred to as grid point) is:

$$\ddot{u}_i = \frac{\int_s \sigma_{ij} n_j ds + F_i}{m} + g_i \quad (15)$$

The acceleration is an integral around the surface s, which encloses the mass m around the grid point. σ_{ij} is the stress tensor and g_i is the gravitational acceleration. F_i is the resultant of all external forces applied on the grid point, and is a sum of three components: (1) F_i^l are the external applied loads. (2) F_i^c are the forces applied from sub-contacts (only applies for grid points along block boundary). (3) F_i^z is the contribution of the internal stress of the zone next to the grid point.

Velocity is calculated by central difference for each vertex, at each explicit time step, by:

$$\dot{u}_i^{(t+\Delta t/2)} = \dot{u}_i^{(t-\Delta t/2)} + \sum F_i^{(t)} \frac{\Delta t}{m} \quad (16)$$

Where the superscripts denote the time at which the corresponding variable is evaluated and:

$F_i^{(t)} =$ Grid point force (out-of-balance force), zero at equilibrium [N]

$\Delta t =$ Time step [sec]

$m =$ Element mass [kg]

Strain ($\dot{\epsilon}$) and rotation ($\dot{\theta}$) related to the grid point displacement during each time step are calculated by the Green-Lagrange small strain tensor:

$$\dot{\epsilon}_{ij} = \frac{1}{2}(\dot{u}_{i,j} + \dot{u}_{j,i}) \tag{17}$$

$$\dot{\theta}_{ij} = \frac{1}{2}(\dot{u}_{i,j} - \dot{u}_{j,i}) \tag{18}$$

Using the appropriate constitutive relations, we can obtain the stress increments (see 2.1.3 for more information about constitutive models). The stress-strain relation is given by:

$$\Delta\sigma_{ij}^{e} = \lambda\Delta\epsilon_{v}\delta_{ij} + 2\mu\Delta\epsilon_{ij} \tag{19}$$

Where:

$\lambda, \mu =$ Lame constants [Pa].

$\Delta\sigma_{ij}^{e} =$ Elastic increments of the stress tensor [Pa].

$\Delta\epsilon_{v} =$ Increment of volumetric strain.

$\Delta\epsilon_{ij} =$ Incremental strains.

δ_{ij} = Kronecker delta function.

Mechanical damping

Adaptive global damping is applied to deformable blocks to absorb kinetic energy. This numerical "servo-mechanism" adjusts the damping automatically, using viscous damping forces that are continuously adjusted, so that the energy absorbed by damping is a constant proportion of the rate of change of kinetic energy.

2.1.3 Constitutive model

Rock mass response to internal and external loads primarily depends on the constitutive models of both the intact rock and the joints intersecting the medium. This section will

briefly introduce the basic concepts of the constitutive models that have been used in this research.

Intact block constitutive model

The intact material in this research is assumed elastic isotropic, i.e. stress-strain laws are linear and path-independent. This model was preferred to Mohr-Coulomb plasticity model because it is the simplest form of material behavior and, in this research, failure occurs exclusively on joints while intact rock deforms elastically under the applied thermal stresses but never reaches material failure. Another reason for choosing the elastic isotropic model is that it only requires three material properties instead of six parameters required for the Mohr-Coulomb plasticity model.

In this model, stress increments depend on strain increments according to the linear and reversible Hooke's law shown in eq. 19 (ITASCA Consulting Group Inc., 2013c).

Joint constitutive model

The model chosen to represent the material behavior of discontinuities in this research is the Coulomb-Slip joint model (ITASCA Consulting Group Inc., 2013c). This model represents a linear joint stiffness and joint shear strength (yield limit, Figure 2.3), based on the joint normal and shear stiffness (K_n, K_s) and friction angle (ϕ). This model also allows consideration of interface cohesion, tensile strength and dilation angle, which in this research are all assumed zero. The interfaces modeled here are preexisting with no connecting forces between them, hence the zero cohesion and tensile strength; the discontinuities are perfectly smooth and hence the zero dilation angle. In addition, no surface degradation is assumed after the onset of plastic sliding across the interfaces.

According to Coulomb friction law, the maximum shear force allowed before plastic deformation is:

$$F^s_{max} = F^n \tan \phi \tag{20}$$

Where F^n is the normal force applied on the joint. When the shear force (F^s) applied to the joint exceeds the force limit (F^s_{max}), shear failure will occur, and the shear force (F^s_i, eq. 14) will update again as follows:

$$F^s_i = F^s_i \frac{F^s_{max}}{F^s} \tag{21}$$

Since dilation is not allowed, no update in the normal force is needed.

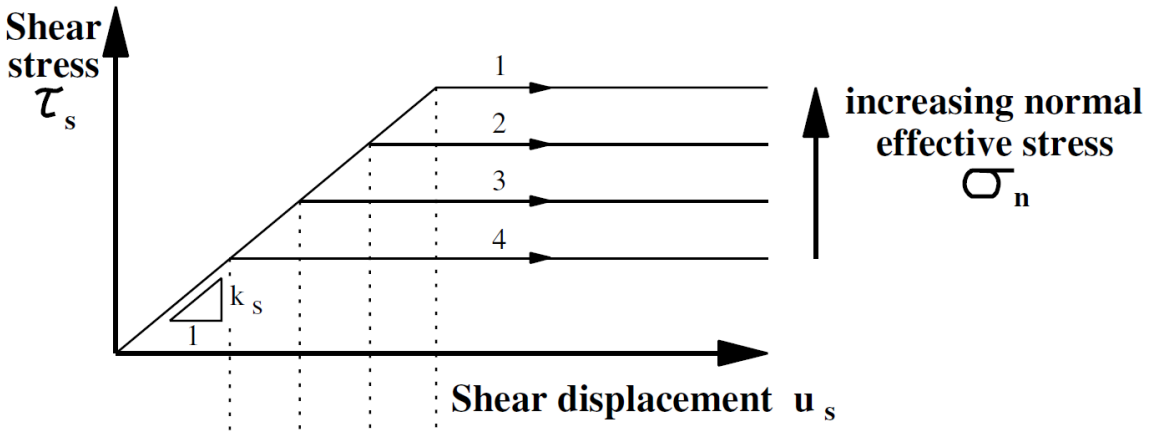

Figure 2.3 - Coulomb slip-joint model (ITASCA Consulting Group Inc., 2013c)

2.1.4 Verification problem – sliding under gravity loading

A 3DEC verification using a simple problem of block sliding on an inclined plane is presented below for a frictional interface subjected to gravitational loading only. The model is presented in Figure 2.4. The inclination angle of the sliding plane is $\alpha = 25°$, and the friction angle of the interface is $\phi = [5°, 10°, 15°, 20°]$. The displacement of the block down the sliding surface, for $t = 1\ second$, is given by:

$$d(t) = \frac{1}{2} g(\sin\alpha - \cos\alpha \tan\phi) t^2 \tag{22}$$

Where g is the acceleration of gravity.

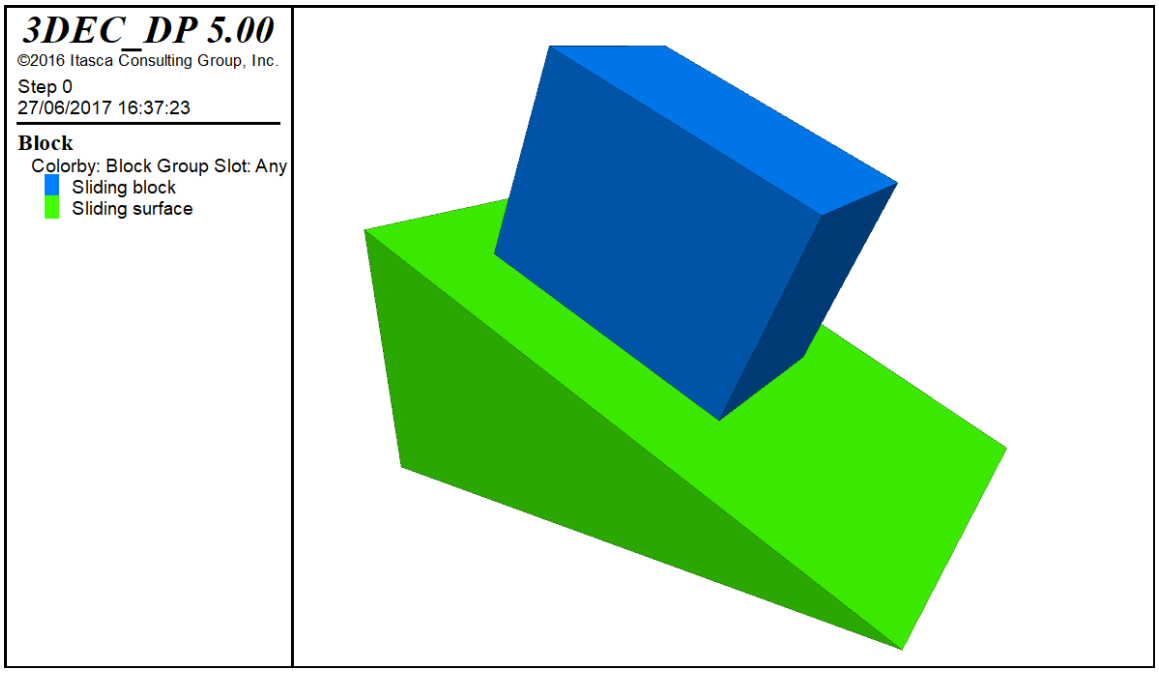

Figure 2.4 - Model configuration for sliding on an inclined slope verification

3DEC simulations (Appendix A) of the problem were performed on the model presented in Figure 2.4, after initial equilibrium has been achieved (the sliding block starts at rest). The numerical input parameters are summarized in Table 1. To prevent internal deformation of the blocks during sliding, both blocks are assumed rigid in this verification.

Table 1 - 3DEC model numerical data, sliding on an inclined slope

Parameter	***Symbol***	***Units***	***value***
Shear stiffness	K_s	GPa/m	0.5
Normal stiffness	K_n	GPa/m	5
Damping factor	β	-	0
Time step	Δt	Seconds	1.4752E-4

A good agreement between the numerical (3DEC) and the analytical solution has been obtained (Figure 2.5). The numerical error (e_N, defined in eq. 23) at the end of the sliding ($t = 1sec$) is 0.1% to 0.2%.

$$e_N = \left|\frac{d_A - d_N}{d_A}\right| \cdot 100\% \quad (23)$$

Where d_A and d_N is the analytical and numerical solutions, respectively.

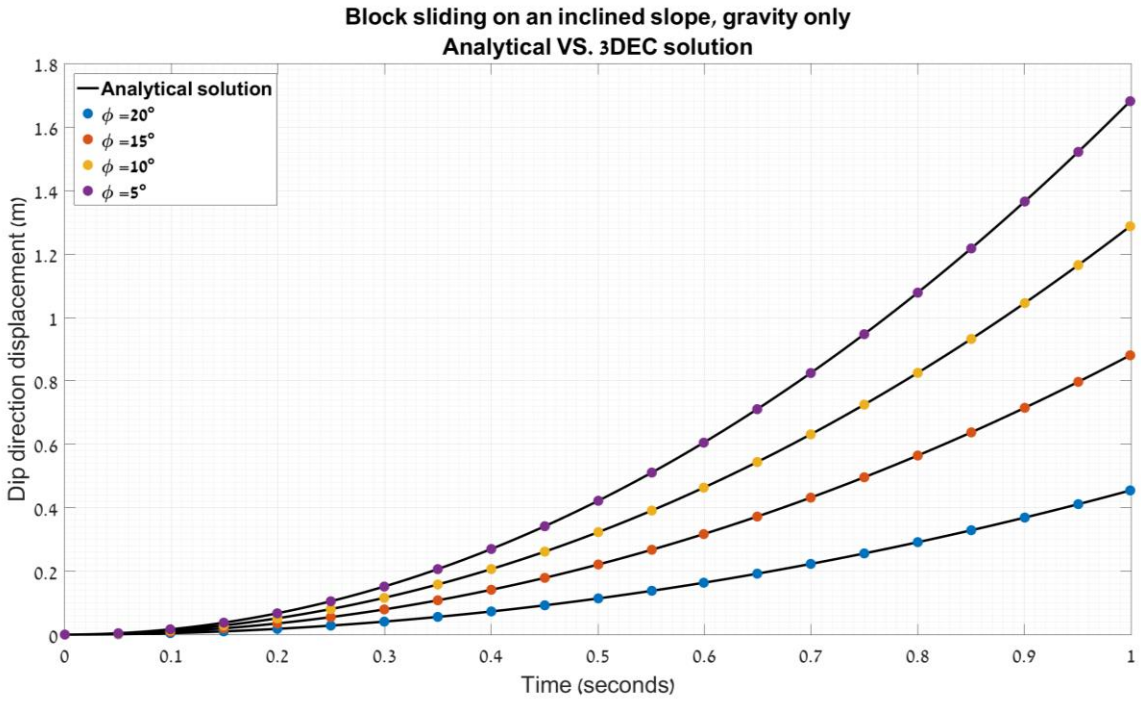

Figure 2.5 - Sliding block displacement vs time for friction angles ranging between 5°-20°.

2.2. Heat conduction in 3DEC

3DEC allows simulation of transient heat conduction and, consequently, the thermally induced displacements and stresses. Thermal volumetric strains are associated with incremental mechanical constitutive laws (eq. 19) to account for thermomechanical coupling (ITASCA Consulting Group Inc., 2013d).

2.2.1 3DEC thermal formulation

Fourier's law of heat conduction is solved in 3DEC using an explicit finite difference method based on medium discretization to tetrahedral zones (2.1.1). A linear temperature gradient is assumed within each tetrahedron (ITASCA Consulting Group Inc., 2013d), as follows:

$$T_{,j} = -\frac{1}{3V}\sum_{l=1}^{4} T^{l} n_j^{(l)} S^{(l)} \tag{24}$$

Where $n_j^{(l)}$ is the unit vector normal to face l, S is the face surface area and V is the tetrahedron volume.

The temperature difference of node n in time t is:

$$\frac{dT^n}{dt} = -\frac{1}{\sum[mC_p]^n}\left[Q_T^n + \sum Q_{app}^n\right] \tag{25}$$

where m is the mass, C_p the specific heat, and Q_T^n are the global nodal values of heat (out-of-balance heat):

$$Q_T^n = C_{nj} T^j \tag{26}$$

where C_{nj} is the global matrix and T is the global vector of nodal temperatures.

$\sum Q_{app}^n$ is the known contribution of applied heat sources, and is irrelevant for this research (no heat sources in the host rock are assumed).

Eq. 25 for all nodes forms a system of ordinary differential equations, solved in 3DEC using an explicit finite difference scheme. The temperature at a node is assumed to vary linearly over a time step Δt:

$$T_{<t+\Delta t>}^n = T_{<t>}^n + \Delta T_{<t>}^n \tag{27}$$

where:

$$\Delta T_{<t>}^n = \chi^n\left[Q_{T<t>}^n\right] \tag{28}$$

$$\chi^n = -\frac{\Delta t}{\sum[mC_p]^n} \tag{29}$$

When using the explicit scheme, to ensure convergence, the time step Δt must be sufficiently small and, based on empirical results, should be constrained by the following expression:

$$\Delta t \leq \frac{1}{m}\frac{L_c^2}{D_T} \tag{30}$$

where D_T is the thermal diffusivity, m is a constant that depends on discretization, and L_c is the smallest tetrahedron characteristic length, defined as: $\frac{volume}{surface\ area\ exchanging\ heat}$. The thermal strain increment due to thermal expansion is given by:

$$\Delta\epsilon_{ij} = \alpha\Delta T\delta_{ij} \tag{31}$$

Heat transfer is coupled to thermal stress by:

$$\Delta\sigma_{ij} = -3K\alpha\Delta T\delta_{ij} \tag{32}$$

where:

$K =$ Bulk modulus [GPa]

$\delta_{ij} =$ Kronecker delta.

$\alpha =$ Thermal expansion coefficient [1/°C]

$\Delta T =$ Temperature difference [°C]

2.2.2 Verification problem – conduction in a plane sheet

In this section a verification of 3DEC using a problem of heat conduction in a finite slab (modified after ITASCA Consulting Group Inc. (2013d)) is presented. A three-dimensional block of thickness $L = 0.8m$ is heated on the plane $x = 0$ with a prescribed temperature $T = 30°C$ for three different exposure times. The plane $x = 0.8m$ is kept at temperature of zero (see Figure 2.6). The initial temperature of the block is 0. The mathematical expression of the problem is:

$$\begin{cases} \dfrac{\partial T}{\partial t} = D_T\dfrac{\partial^2 T}{\partial x^2}, \quad 0 \leq x \leq 0.8, \quad t \geq 0 \\ T(x,0) = 0 \\ T(0,t) = 30 = T_0 \\ T(0.8,t) = 0 \end{cases} \tag{33}$$

The analytical solution of this problem is given by Carslaw and Jaeger (1959):

$$\frac{T(x,t)}{T_0} = 1 - \frac{x}{L} + \frac{2}{\pi}\sum_{n=1}^{\infty}\frac{1}{n}e^{-\left(\frac{n\pi}{L}\right)^2 D_T t}\sin\frac{n\pi x}{L} \qquad (34)$$

where D_T is the thermal diffusivity of the block.

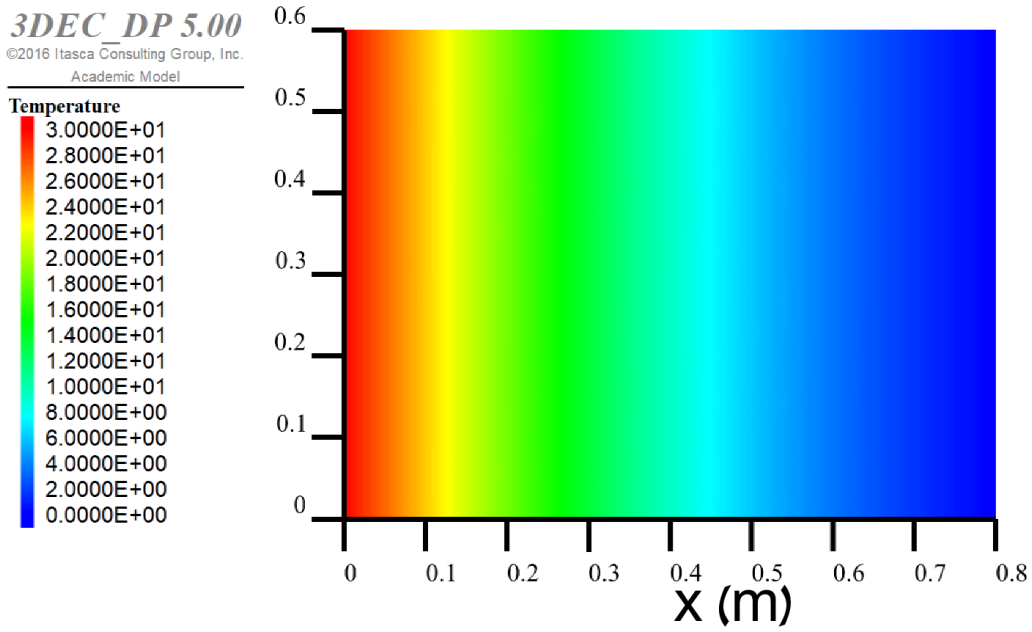

Figure 2.6 - Temperature gradient in a block

Temperature distribution profiles in the block are presented in Figure 2.7 for three different exposure times. The numerical solutions closely match the analytical solution. We find that the numerical solution is independent of tetrahedron size or thermal time step (Appendix B).

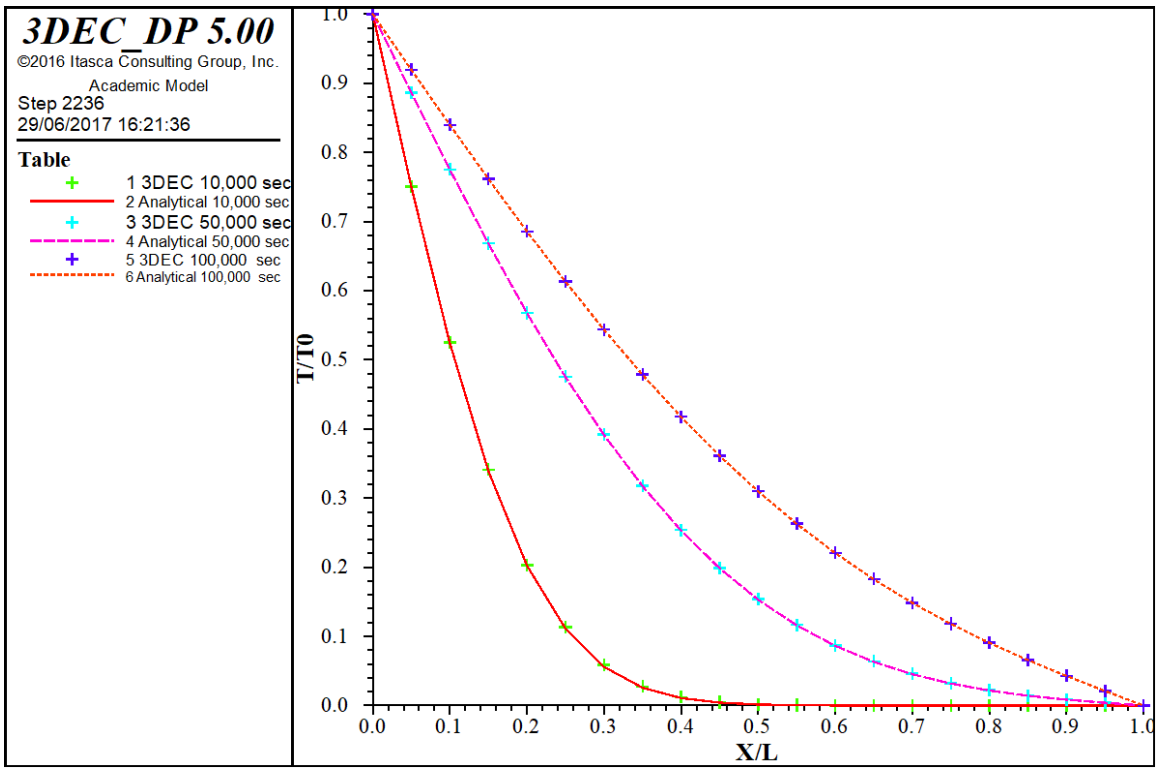

Figure 2.7 - Comparison between analytical (lines) and numerical (crosses) solutions for heat conduction in a plane sheet. Three different exposure times of the block to a constant temperature at x/L=0. The other end (x/L=1) is kept at zero temperature.

Chapter 3 - Validation of the wedging-ratcheting mechanism with 3DEC using physical test results

The research presented in this thesis is divided into two parts: (1) numerical calibration using laboratory experiments, and (2) examination of a case study from Mount Masada, Israel. As the main tool of examination in this study is numerical, we must verify our results with known solutions. Part of this process has been described earlier, in the mechanical (section 2.1.4) and thermal (section 2.2.2) verifications. However, an examination of a real case study requires a coupled thermo-mechanical approach, which was not compared with an analytical solution in the previous chapter, as there is no such solution available. Instead, we compare the numerical results with experimental results obtained from a physical model in a climatically controlled room. We then use the same numerical control parameters as calibrated in the validation study, in the analysis of the case study. A flowchart summarizing the working procedure is presented in Figure 3.1.

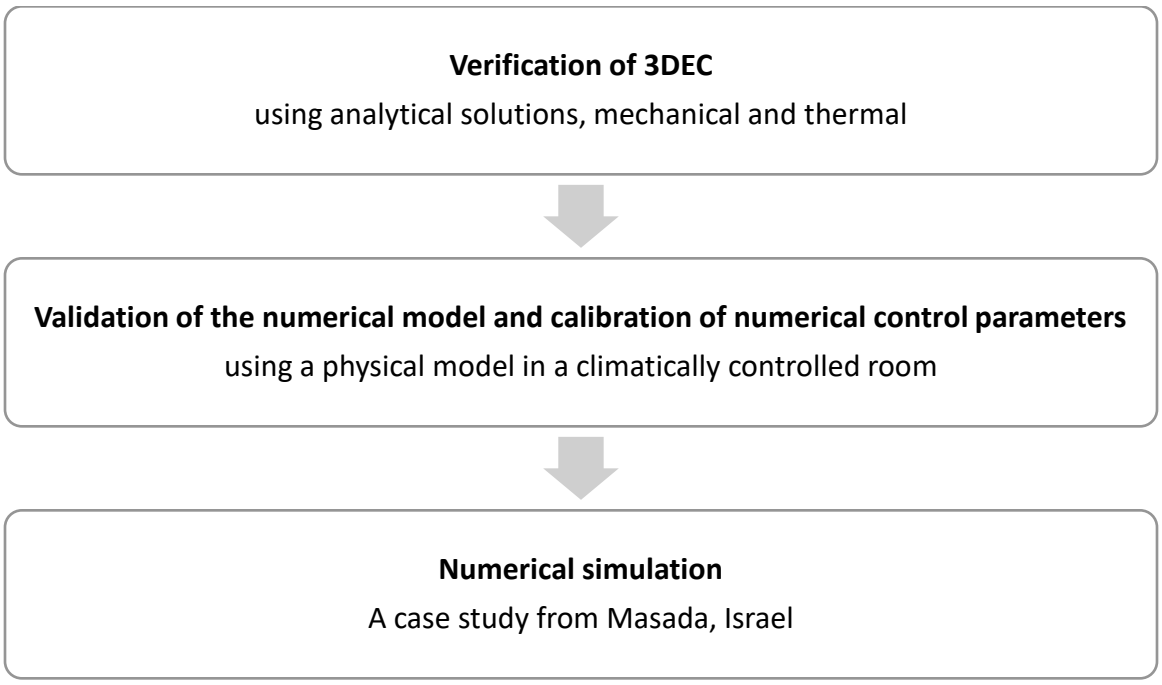

Figure 3.1 - The working procedure of this research

In his work, Feldheim (2017) – an M.Sc. student of the rock mechanics research group at BGU – modeled the proposed wedging-ratcheting mechanism experimentally using a

physical model. He built a large-scale concrete model (Figure 3.2) and conducted experiments in a climatically controlled room, to check the validity of the mechanism and the analytical solution suggested by Pasten (2013).

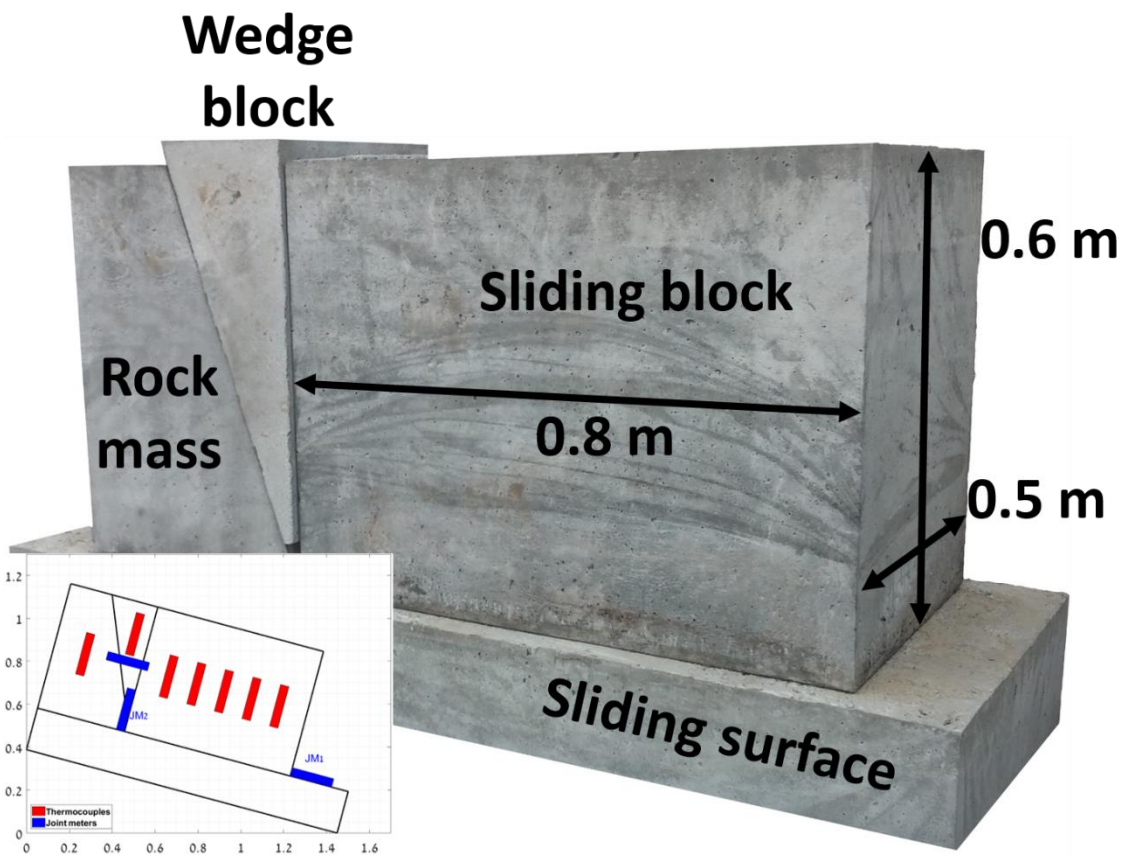

Figure 3.2 - Concrete physical model (Feldheim, 2017). A sketch denoting the locations of the thermocouples and the joint meters is presented in the lower left corner (length in meters).

3.1. Thermomechanical properties of the concrete

Prior to the experiments in the climatically controlled room, a few tests were designed to find the thermal properties of the concrete. In addition, triaxial and direct shear tests were performed to determine the mechanical properties of the concrete material.

3.1.1 Thermal diffusivity

A block of concrete of length of 28 cm was subjected to a constant temperature of $50\ °C$ on its opposing faces. Seven thermocouples were installed in the concrete during its

solidification (Figure 3.3). To minimize heat flow through the side of the block, the block was covered with an isolation foam.

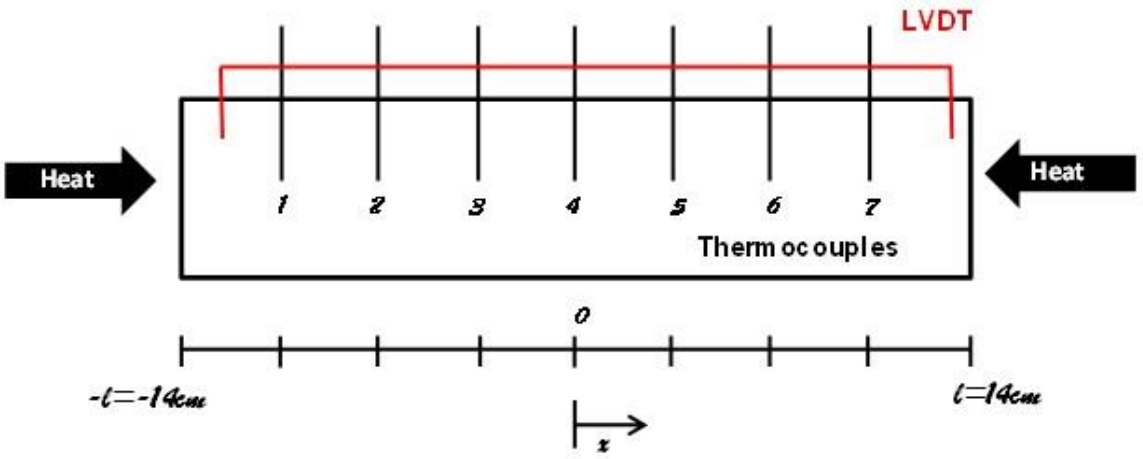

Figure 3.3 - Model sketch for experimental determination of thermal diffusivity.

During the experiment, a data logger records the temperature of all thermocouples with a time interval of one minute. Average values of two opposing thermocouples at the same location relative to the center (e.g. 1 and 7, 2 and 6, etc.) were calculated. The concrete temperature relative to the boundary temperature was plotted as a function of the relative location (dimensionless plot), for every hour. These curves were compared to time factor (T) curves plotted using the following equation (Carslaw and Jaeger, 1959):

$$\frac{v}{V} = 1 - \frac{4}{\pi}\sum_{n=1}^{\infty}\frac{(-1)^n}{2n+1}e^{-\frac{(2n+1)^2\pi^2 T}{4}}\cos\frac{(2n+1)\pi x}{2l} \qquad (35)$$

where:

$v =$ Thermocouple temperature, $°C$

$V =$ Boundary temperature, $°C$

$x =$ Thermocouple location, m

$l =$ Block half-length, m

T = Time factor, dimensionless, depends on thermal diffusivity ($\kappa, \frac{m^2}{sec}$), time (t, sec), and block length (l, m):

$$T = \frac{\kappa t}{l^2} \tag{36}$$

Correspondence curves for several values of time factor (T) were matched to the temperature profiles in the block that were recorded during the test (Figure 3.4). Thermal diffusivity was then calculated using the time elapsed and the corresponding time factor (Table 2).

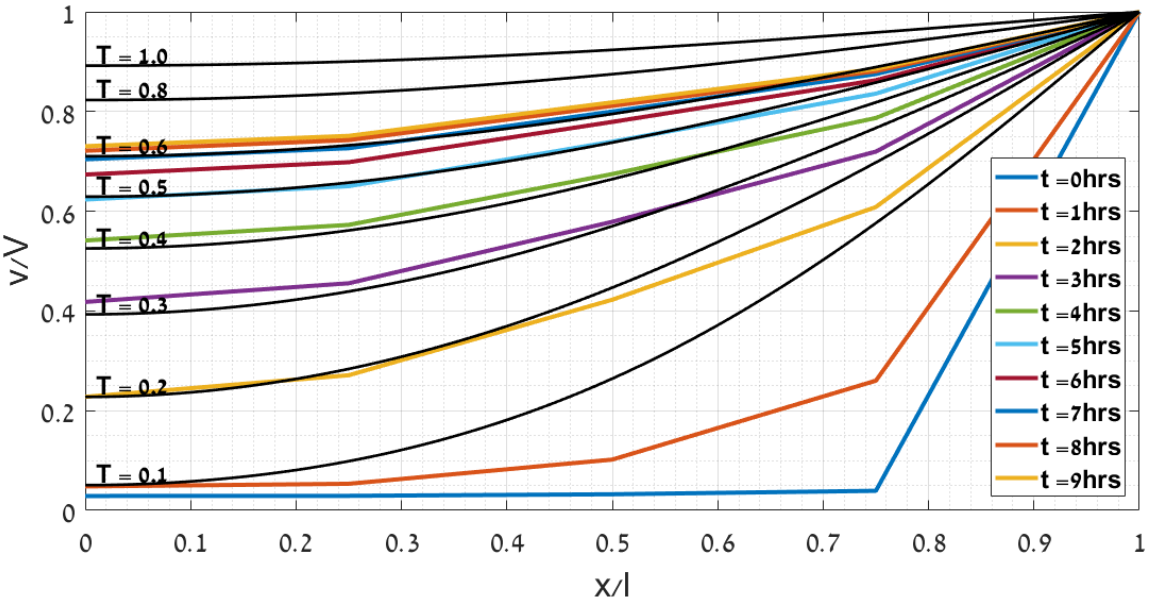

Figure 3.4 – Temperature profiles in the block after several periods of heating (colors) and time factor curves plotted using eq. 35.

Table 2 - Thermal diffusivity calculation.

T	***t (seconds)***	$\boldsymbol{\kappa\ (10^{-7}m^2/sec)}$
0.3	3*60*60	5.444
0.5	5*60*60	5.444
0.6	6*60*60	5.444

This experiment suffers from some inaccuracies. Even though the concrete beam was covered with the insolation foam, heat could still flow through the block boundaries. The actual thermal diffusivity, therefore, can be expected to be greater than the diffusivity obtained in the laboratory experiment.

3.1.2 Thermal expansion coefficient

The same block, a diagram of which is presented in Figure 3.3, was heated in an oven to reach a uniform temperature of $50°C$. Then, it was put in a room under ambient temperature of approximately 20°C. Potentiometer displacement transducer recorded the block contraction as it cooled under ambient temperature. The block cooled relatively uniformly, and an average of all seven thermocouples was calculated. An average of 10 temperature measurements at roughly one-hour intervals is used to plot Figure 3.5.

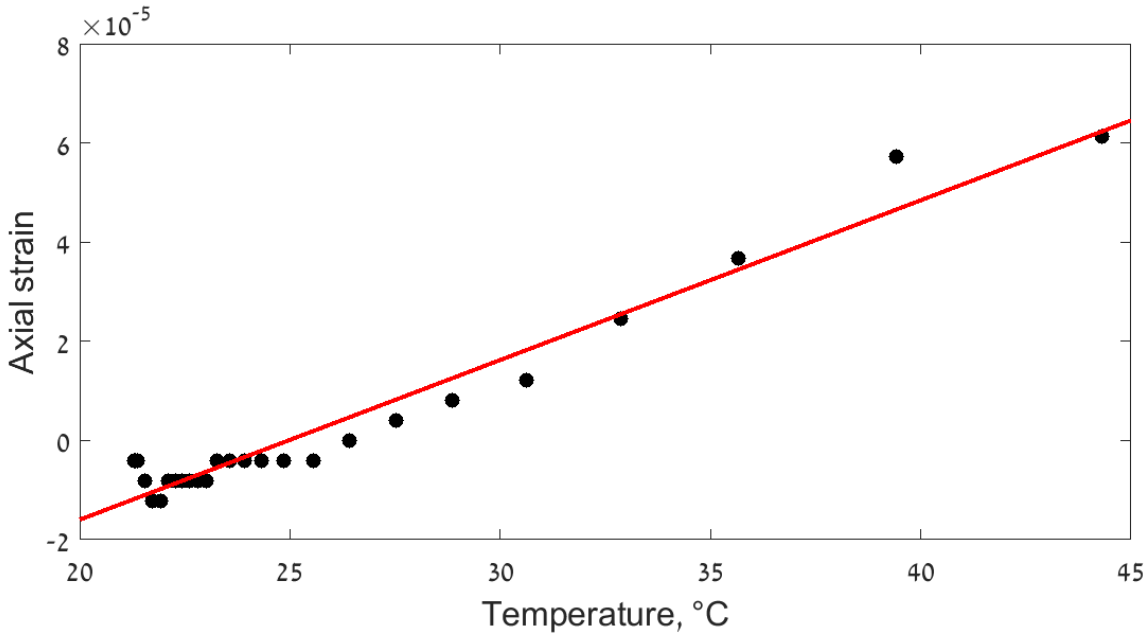

Figure 3.5 - Axial strain vs. average temperature in cooled block. The thermal expansion coefficient is the slope of the linear trend line.

The linear thermal expansion coefficient (α_L) was calculated using the following equation (the slope of the trend line):

$$\alpha_L = \frac{dL}{L}\frac{1}{dT} = 3.16 \cdot 10^{-6} \tag{37}$$

where:

$\frac{dL}{L}$ = Axial strain

dT = Temperature change, °C

3.1.3 Uniaxial compression test

A uniaxial compression test was performed using a TerraTek triaxial testing system, model FX-S-33090. The stiff load frame operates using a closed-loop, servo-controlled hydraulic piston of maximum axial force of 1.4 MN and stiffness of 5x10^9 N/m. The results of this test are presented in Figure 3.6.

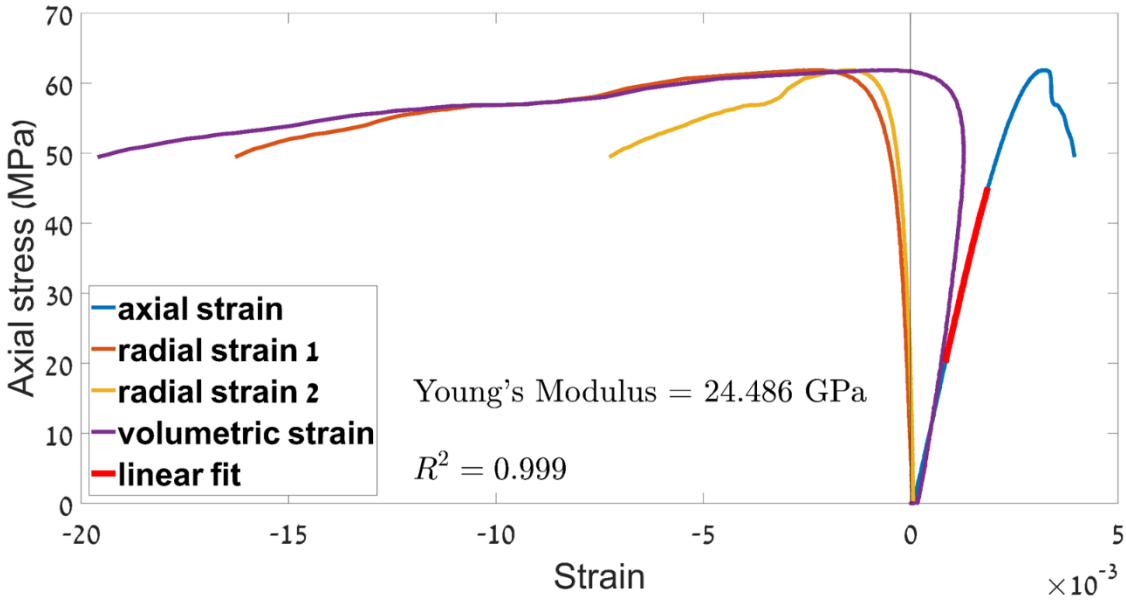

Figure 3.6 - Uniaxial compression test results of the concrete used in the physical model. A red line marks the elastic region from which the Young's Modulus was determined.

Young's Modulus (E) is defined as the ratio between the axial stress and the axial strain in the elastic region, and is calculated by the slope of the linear fit of the stress-strain curve, so that $E = \frac{\sigma_{axial}}{\epsilon_{axial}} = 24.486\ GPa$.

Poisson's ratio (ν) is calculated by the slope of the linear fit of the mean radial strain vs. axial strain curve in the elastic region, so that $\nu = \frac{\epsilon_{radial}}{\epsilon_{axial}} = 0.2513$ (Figure 3.7).

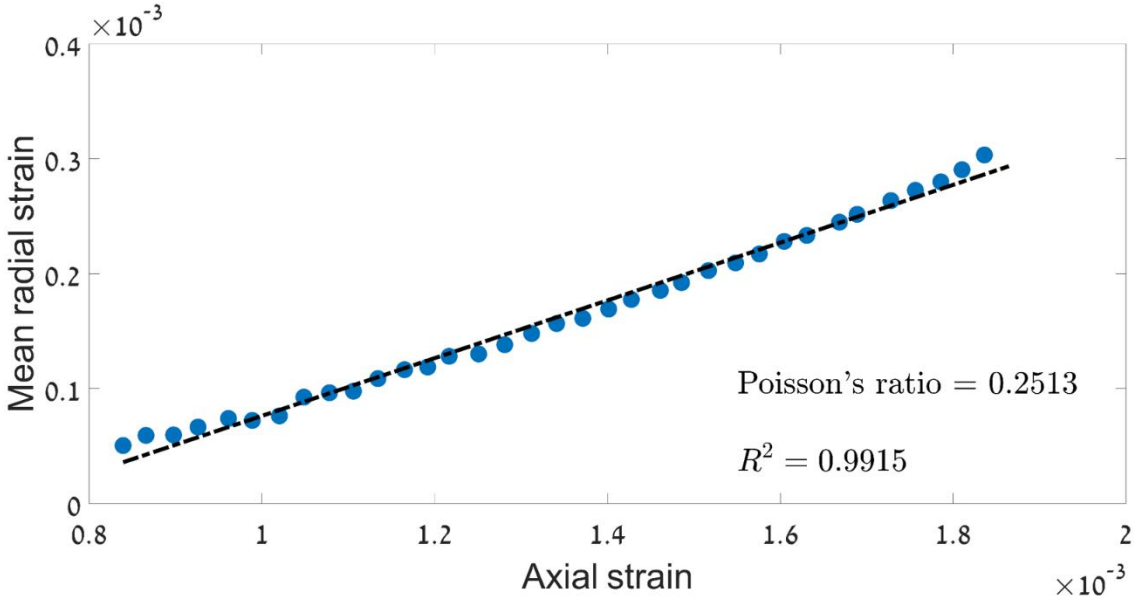

Figure 3.7 – Mean radial strain vs. axial strain in the uniaxial compression test. Poisson's ration is defined as the slope of the linear fit of the curve in the elastic region.

3.1.4 Direct shear

Joint parameters of the concrete-concrete interface were determined using two different direct shear apparatus:

(1) A hydraulic, closed-loop, servo-controlled, direct shear system manufactured by TerraTek Systems, consisting of two servo-controlled pistons with normal and shear load capacities of 1000 kN and 300 kN, respectively. Vertical and horizontal displacements are monitored by four and two LVDT transducers, respectively, each of 50 mm range and 0.1% linearity full scale. Direct shear tests were performed under an imposed constant normal stress condition and once the normal load target was reached the interfaces were sheared under a controlled displacement rate to a target distance of 2 mm. Once the target displacement was reached the normal stress was elevated to a new target and shear resumed. These normal and direct shear test segments were repeated several times. A plot of the normal segments is shown in Figure 3.8. The normal stiffness (K_n) is calculated in Figure 3.8 by the slope of the elastic region of the normal stress (σ_n) - vertical displacement (u_v) curve, so that $K_n = \frac{\sigma_n}{v} = 5MPa/mm$.

(2) Low load Digital Shear Machine, manufactured by ELE International, used to resolve as accurately as possible the shear stiffness for the tested concrete interfaces. Normal stress is applied in this test manually, by adding weights. After the normal stress is applied, shear force is applied to the shear box. Vertical and horizontal displacements are monitored by two LVDT's. Shear stiffness (K_s) is extracted from the slope of the shear stress (τ) - horizontal displacement (u) curve for each normal stress segment in both experimental settings.

Direct shear tests using both apparatuses allow us to determine joint parameters over a wide range of normal stresses. Since shear stiffness is dependent on the applied normal stress, a linear regression is used in Figure 3.11 to determine this parameter for the case of the physical model, where the normal stress between the sliding block and the sliding surface is 0.013 MPa, so that $K_s = \frac{\tau}{u} = 0.5\ MPa/mm$.

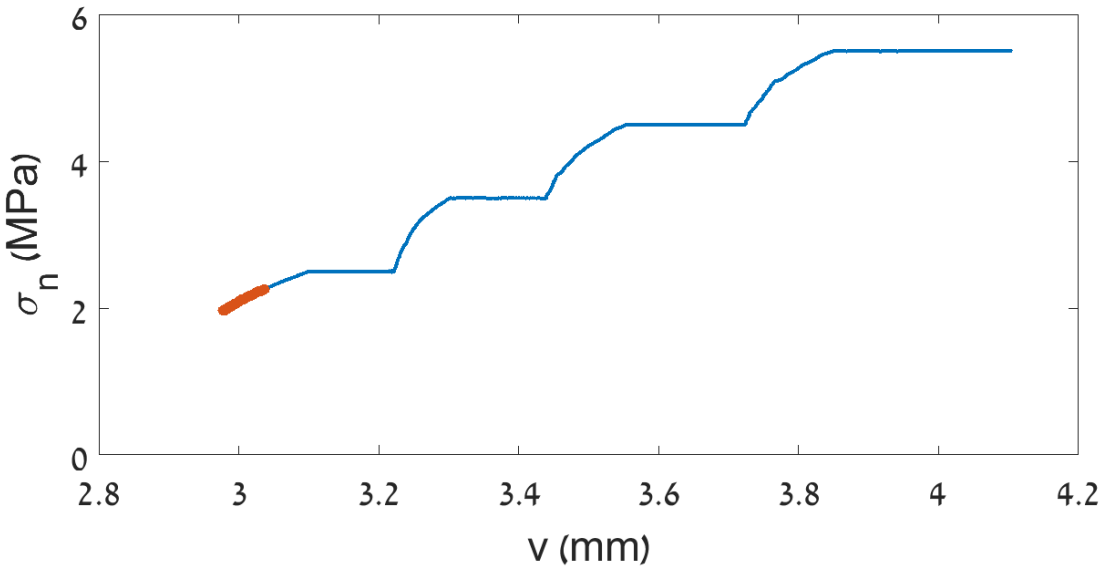

Figure 3.8 - Normal stress vs. vertical displacement. The Normal stiffness is defined as the slope of this curve in the elastic region (red line).

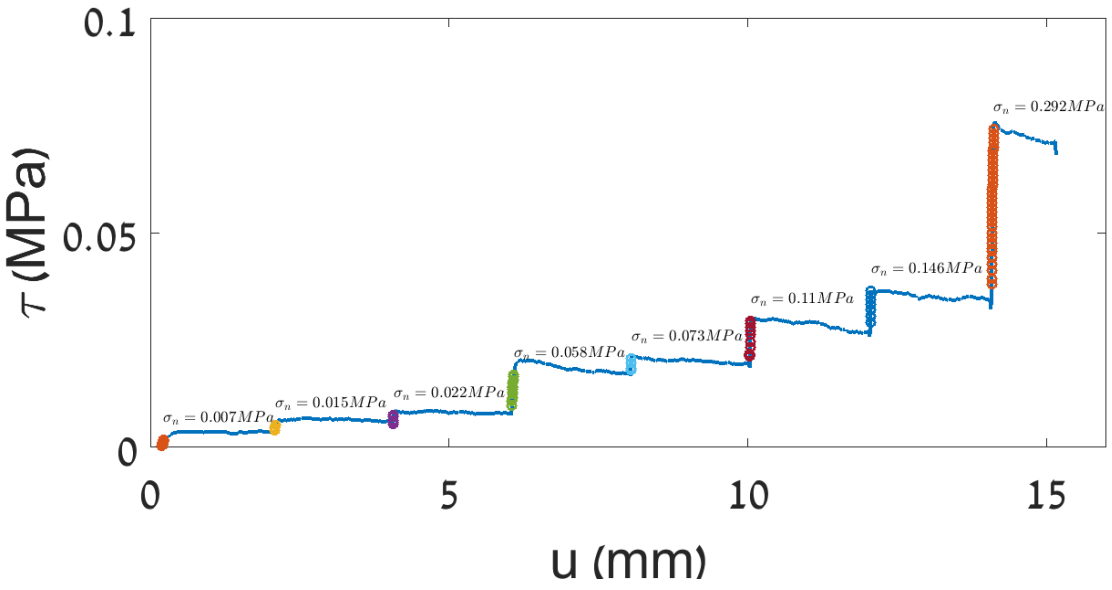

Figure 3.9 – Direct shear tests with the low force ELE system

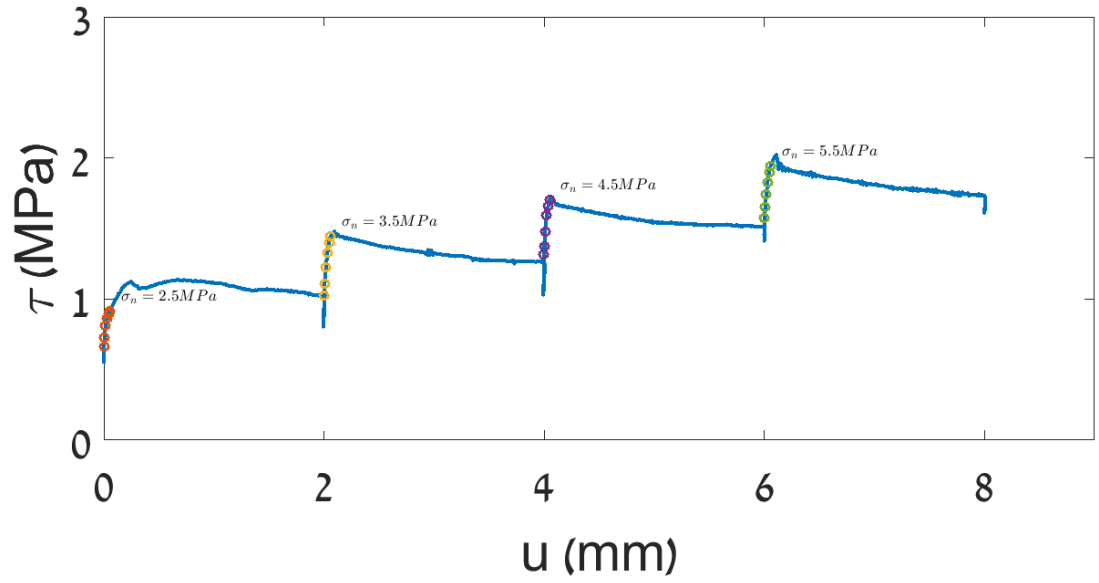

Figure 3.10 – Direct shear tests with the high force TerraTek system.

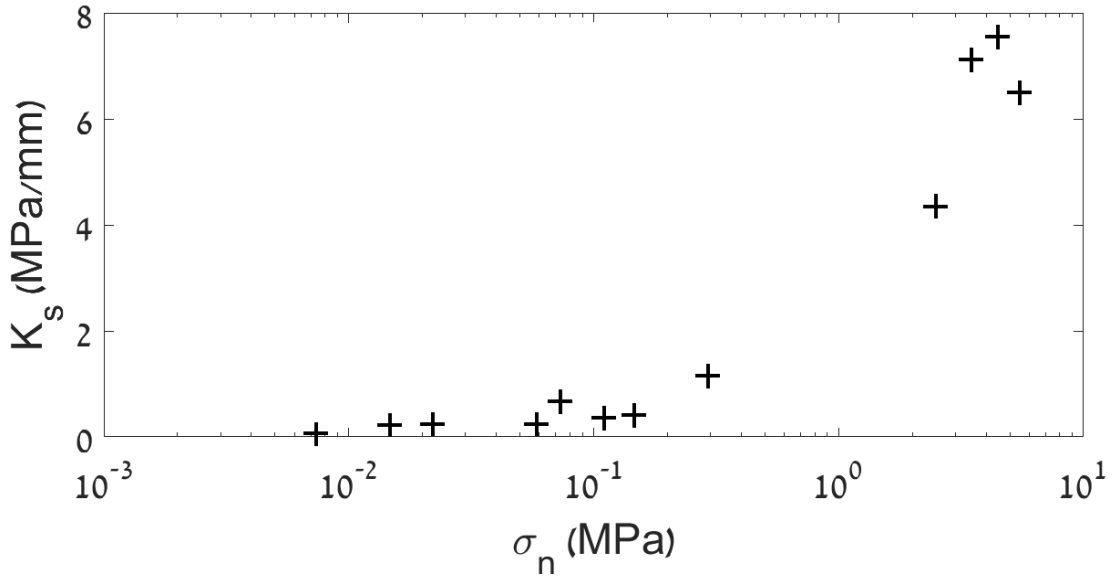

Figure 3.11 - Shear stiffness vs. normal stress.

The friction angle for the tested concrete interfaces was determined from the results of the servo-controlled tests using linear regression and assuming Coulomb friction. The representative friction coefficient is thus the slope of the linear regression curve in Figure 3.12.

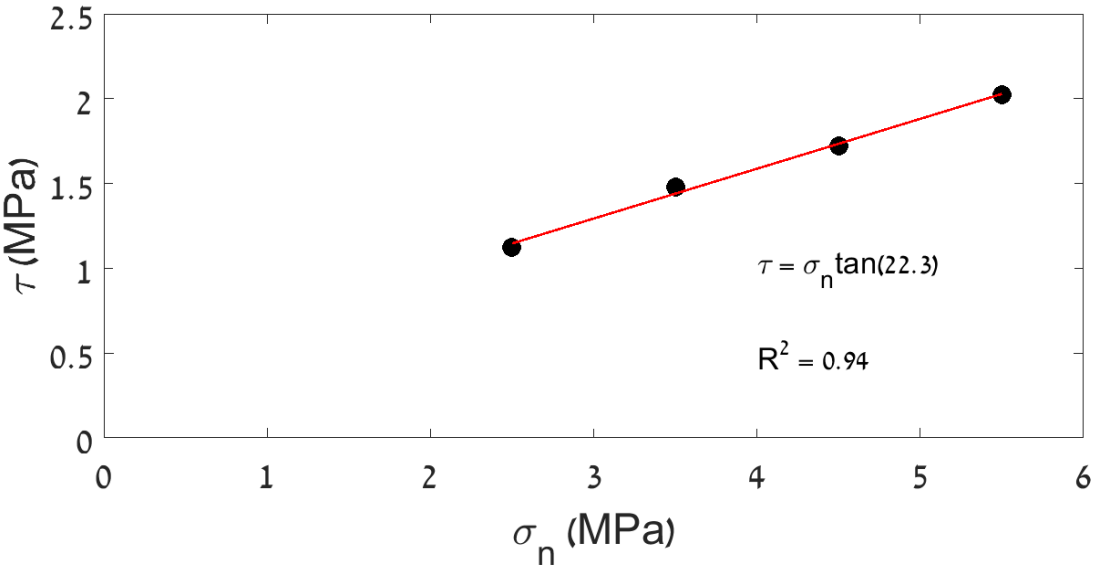

Figure 3.12 – Results of segment direct shear tests performed on the concrete interface in peak shear stress – normal stress space

3.2. Experimental settings in the climatically controlled room

The physical model shown in Figure 3.2 was transferred to a climatically controlled room, where the experiments were carried out. The sliding surface was connected to a table inclined 15° with respect to the horizontal. The rock mass and the sliding surface were fixed during the experiment, and the wedge and the sliding block were free to move.

During concrete preparation and solidification, thermocouples were installed inside the sliding block and the wedge block to monitor temperature propagation during the experiments. Two types of displacement monitoring devices were used to track sliding block and wedge displacement: (1) Vibrating Wire crack meter (VW) with a range of 15 millimeters and non-linearity of 0.09% full scale, and (2) potentiometer with a range of 10 millimeters and non-linearity of 0.1% full scale.

Since displacement meters may be sensitive to temperature changes, at each location both types of displacement meters were installed (see Figure 3.2 for thermocouples and displacement meters configuration). The displacement meters measuring the wedge displacement were positioned on opposing sides of the model. In addition, a high-resolution camera tracked the displacement across the joint that separates the sliding block and rock mass. A data logger (CR 1000) recorded all data and stored it in a computer. The course of the experiment was as follows:

1. Room temperature increased to 35°C.
2. Block temperature equilibrates with room temperature (uniform temperature distribution).
3. Room temperature decreased to 5°C.
4. Block temperature equilibrates with the new room temperature (uniform temperature distribution).
5. Data logger records displacement and room temperature every three minutes.
6. Next cycle of heating and cooling is initiated, etc.

Thermo-mechanical properties of both intact concrete and concrete-concrete interface were determined experimentally and the results are summarized in Table 3 below.

Table 3 - Thermo-mechanical properties of the concrete used for experiments

	Parameter	***Symbol***	***Units***	***Value***
Material properties	Elastic modulus	E	GPa	24.486
	Poisson's ratio	ν	-	0.2513
	Bulk density	ρ	Kg/m^3	2140
Joint properties	Friction angle	ϕ	°	21.28
	Normal stiffness	K_n	GPa/m	5
	Shear stiffness	K_s	GPa/m	0.5
Thermal properties	Thermal expansion coefficient	α	10^{-6}/°C	3.16
	Thermal diffusivity	D_T	10^{-7}m^2/sec	7.82
	Specific heat capacity (assumed)	C_p	J/kg/K	850

3.3. 3DEC validation

Mechanical and thermal verifications for 3DEC using analytical solutions were presented and discussed in sections 2.1.4 and 2.2.2. The physical model is used to calibrate and validate thermo-mechanical computations with 3DEC.

The physical model geometry was reproduced in 3DEC as shown in Figure 3.13; the simulation code is provided in Appendix D. Blocks were discretized using a uniform mesh with an average edge length of 4 cm; for discussion of the sensitivity of the code to mesh and element size see section 3.4. Thermo-mechanical properties were assigned to the concrete and the interfaces as listed in Table 3, and boundary conditions, in particular the temperature time-histories, were applied on all exposed faces of the three-dimensional model. The model is fixed in the normal direction behind the rock mass, and in all directions at the bottom of the sliding surface. 3DEC simulations (see 3DEC code in Appendix C) began after initial equilibrium was obtained. Before any thermal loading, and under gravity only, the model was adjusted to block cutting, mesh generation, and to the applied boundary conditions. An elastic stress field was applied by running the model until force equilibrium was reached (Figure 3.14). During that process, blocks were settled, and

displacement took place across the joints. The unbalanced force (eq. 16) and the settlement of the sliding block as obtained for the vertex shown by red point in Figure 3.13, were used to monitor the "stepping to initial equilibrium" phase.

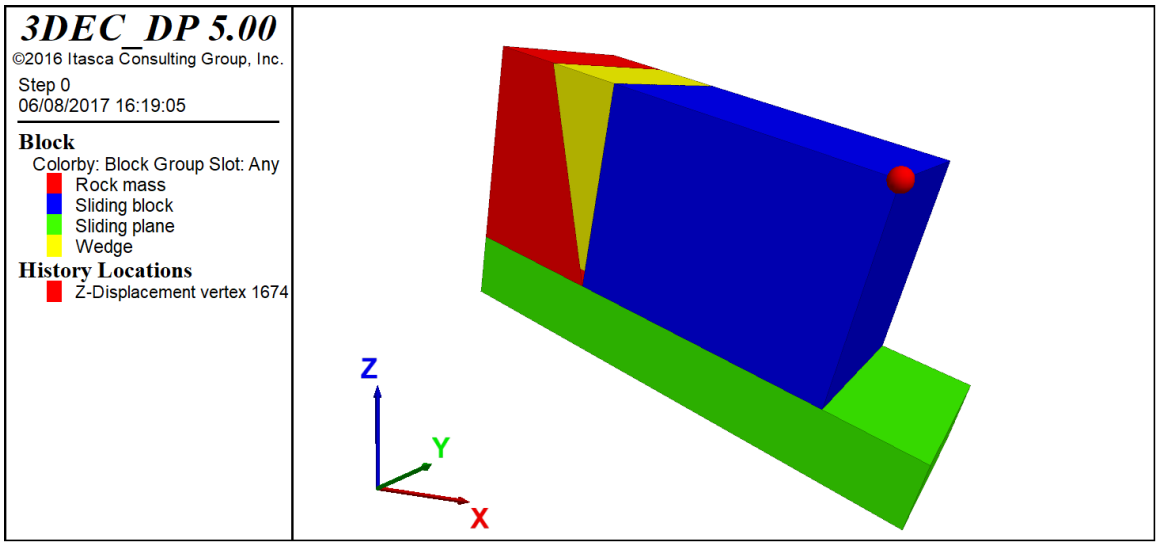

Figure 3.13 – Wedging-ratcheting 3DEC model. Location of sliding block settlement marked with a red sphere.

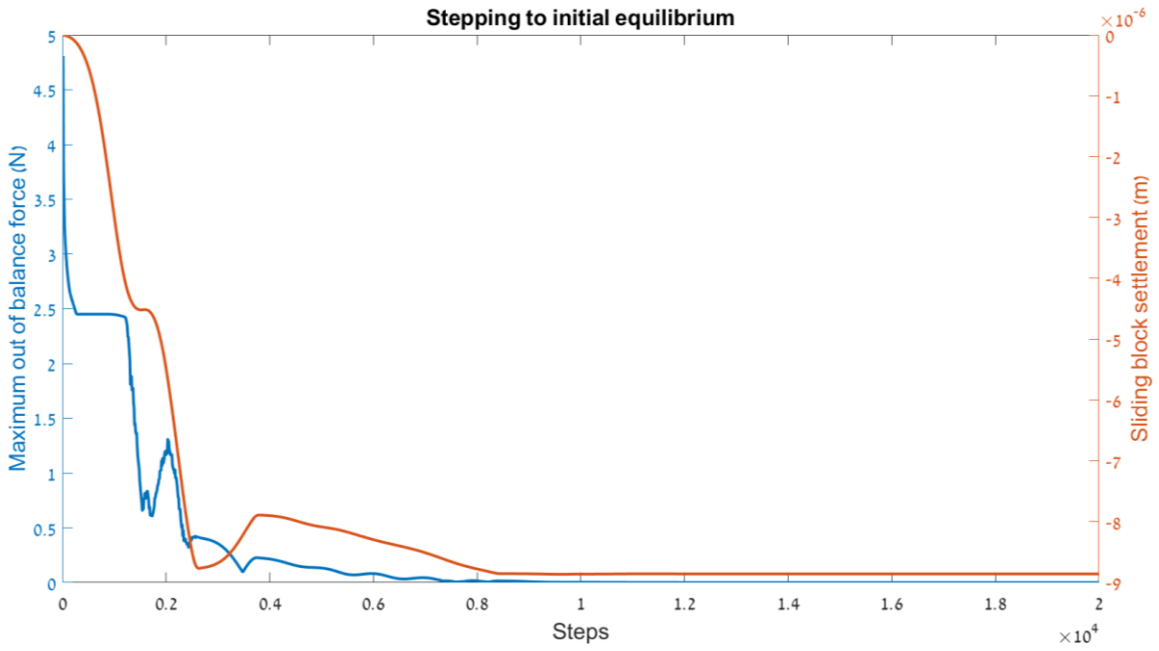

Figure 3.14 - Model stepping to equilibrium. The left vertical axis (blue) is the maximum unbalanced force in the system (=zero when equilibrium obtained) and the right vertical axis (red) is the vertical displacement of the red sphere in Figure 3.13.

Displacement histories of the sliding block and the wedge were recorded for grid points or sub-contacts at the exact same locations as the displacement meters in the physical model (Figure 3.2).

Displacements of the sliding block and the wedge (displacement meters 1 and 2 in Figure 3.2, respectively) as obtained with 3DEC and in the lab, are plotted in Figure 3.15.

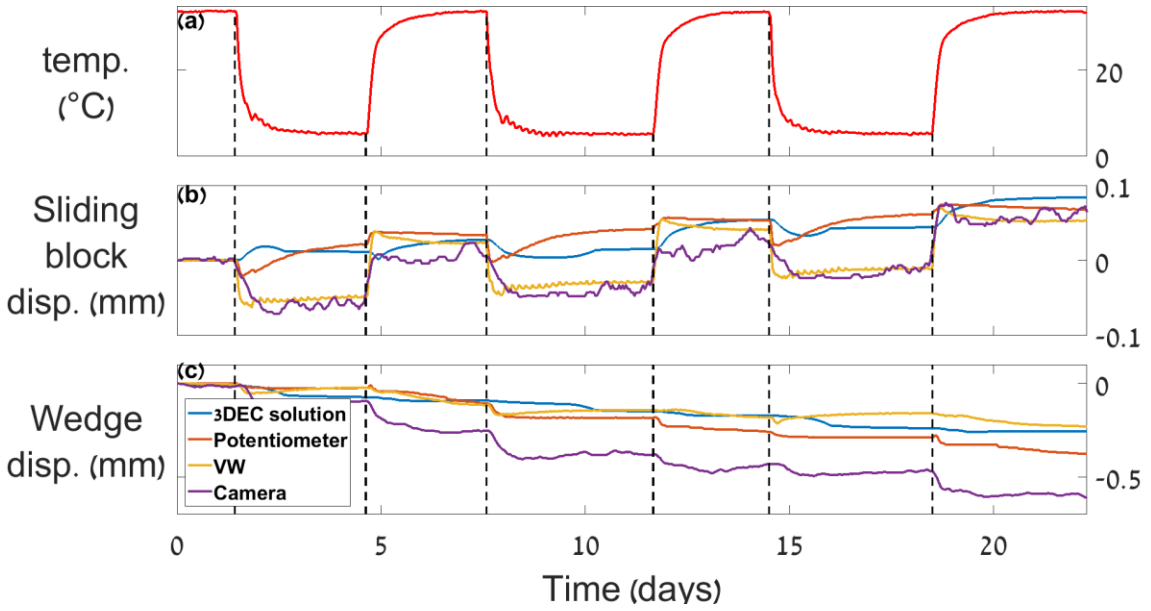

Figure 3.15 - Comparison between lab and numerical results for sliding block (b) and wedge (c) displacements, due to temperature oscillations (a). Output from both types of joint meters and the camera are presented. In figure (b), displacement down the slope is defined as positive. In figure (c), wedge displacement down the opening crack is defined as negative.

The temperature profile of the experiment as shown in Figure 3.15 (a) represents three cycles of heating and cooling, or three whole years (three cycles of summer and winter). The sliding block and the wedge block displacements computed by 3DEC are in accordance with the physical model displacements as obtained with the potentiometer and the VW transducers. When temperature is increased, the sliding block slides down along the sliding surface (Figure 3.15 (b)). As a result, the wedge slides down the opening joint (Figure 3.15 (c)). When temperature drops, the sliding block contracts a bit, allowing the wedge to slide further in the opening aperture. The wedge is not sliding up the joint and the failure continues in the same direction for the consequent cycles. Note that the wedge is sliding down in both heating and cooling phases.

It seems that the Vibrating Wire transducer is more sensitive to temperature changes. When temperature drops, the measurement shows that the sliding block contracts considerably so that the block toe, where VW 1 is located, slides up the surface a significant distance of ~ 0.6 mm. Still, a cumulative displacement down the sliding surface through the thermal cycles is clearly observed, and is equal to both displacement meters output, as well as the camera measurements (Feldheim, 2017).

3.4. 3DEC sensitivity analysis to numerical control parameters

The choice of the numerical control parameters used to validate 3DEC simulations against the laboratory experiment proved not a simple task. We found that the numerical results for different mesh sizes, time steps, and damping factors, could change significantly.

In this section, we study the effect of the numerical control parameters on the cumulative displacement of the sliding block (Figure 3.15 (b)). This displacement was chosen for the sensitivity study because this is the critical displacement that causes slope failure, and because the two displacement meters (VW and potentiometer) are showing the same cumulative displacement (at the end of the experiment and at the end of each cycle).

For all simulations, thermal and mechanical properties of the concrete and the interfaces remain constant. A range of mesh sizes, defined by the average edge length of the tetrahedral zones, was assigned to the model. For shorter edge length, the mesh is finer, and the model contains more zones. The zones in 3DEC are constant strain zones, which means that there is no stress gradient within a single zone. Sufficient discretization needs to be defined in order to represent the expected stress gradient with an adequate accuracy. Thus, a finer mesh should yield a more accurate result.

Twelve mesh sizes were simulated, each with six different time intervals. The mesh size was scaled by the ratio between the tetrahedron length β and the length of the sliding block L_B with ratios β / L_B varying between 2% and 16%. The thermal time step interval was varied between 5 s to 30 s. Clearly, with decreasing element size the numerical solution accuracy is expected to increase, however the CPU time also increases very significantly

with mesh refinement; therefore, a satisfactory balance must be sought. With the aid of the physical model results, the most representative solution can be found.

The results of the sensitivity analysis to element and time step size are presented in Figure 3.16.

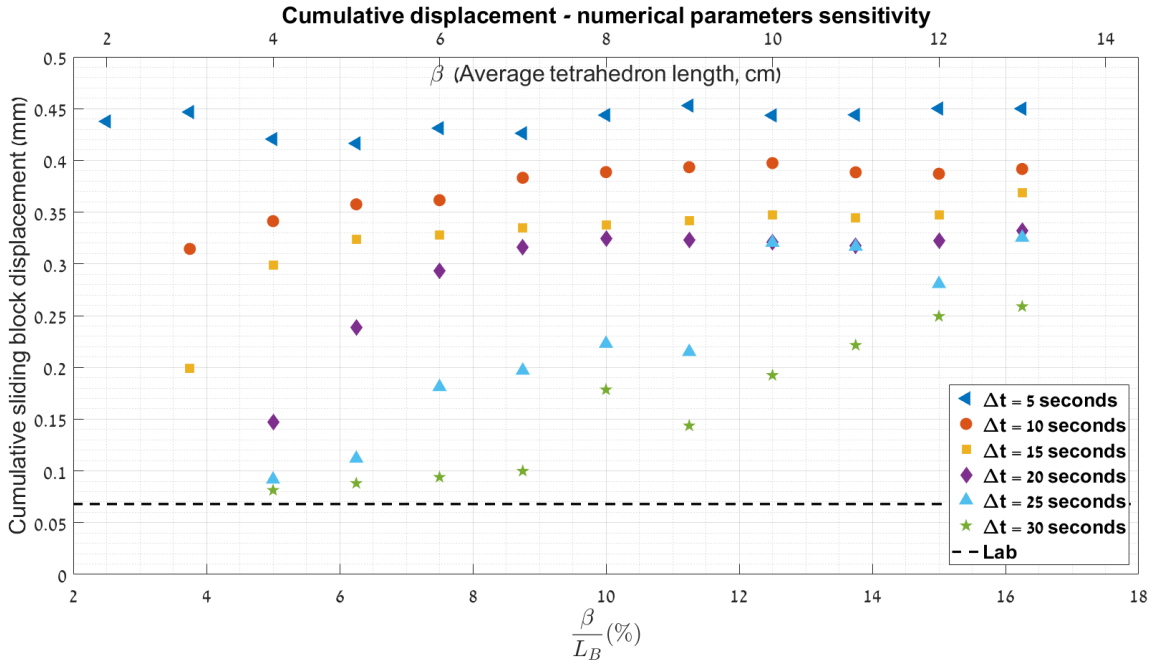

Figure 3.16 – 3DEC simulation sensitivity to numerical control parameters. Different edge lengths (upper horizontal axis) tested for different thermal time steps (colors). The lower horizontal axis expresses the size of edge length relative to sliding block length, in percent. The dashed line is the cumulative sliding block displacement obtained in the laboratory experiment by potentiometer #1.

Inspection of the results displayed in Figure 3.16 reveals that the 3DEC solution is very sensitive to the thermal time step size and less sensitive to the element size. The cumulative displacement is much greater for smaller time steps. Moreover, the discrepancy in displacement between numerical and physical model results increases with decreasing thermal time step. For a constant thermal time step, especially smaller steps, the solution remains almost constant for different mesh sizes. For thermal time steps greater than five seconds, it seems that the solutions converge towards the physical test result with increasing discretization.

There are few possible explanations for the influence of thermal time step and mesh size on the numerical solution:

1. Temperature changes are too rapid for the model to remain in mechanical equilibrium. 3DEC default is to execute one mechanical time step for every thermal time step. When multiple mechanical steps are executed between each thermal cycle, however, the results remain the same.
2. Generation of more zones results in more sub-contacts between elements. Sub-contacts in 3DEC are represented by springs (section 2.1.1). Excess number of springs may generate excess elastic energy as the block slides, adding to the system real energy, resulting in an artificial stresses and displacements, in our case, when the ration is smaller than 5%.
3. For large number of zones, 3DEC solution requires more cycles. Rounding error may become considerable in problems that run for a large number of cycles with a low applied velocity (ITASCA Consulting Group Inc., 2013b).

Considering the results of the sensitivity analyses, we find that a mesh discretized with tetrahedron length of about 5% of the sliding block length in the direction of sliding, namely an edge length of 4 cm, is sufficiently accurate; this mesh can produce valid results based on laboratory experiments. The explicit thermal time step is calculated by eq. 30 and equals to 30 seconds.

3.5. 3DEC sensitivity analysis to thermal and mechanical input parameters

Once an appropriate mesh size and thermal time step were set for this model, and results were validated using laboratory experiments, we can explore the influence of rock thermal and mechanical parameters on the magnitude of displacement and how significant their role is in the wedging-ratcheting mechanism. To avoid solution instability, as discussed in the previous section, the applied temperature was smoothed as follows:

$$T(t) = T_0 + A * \sin \omega t \tag{38}$$

where:

T_0 = Initial temperature ($= 20°C$)

A = Amplitude ($= 15°C$)

ω = Daily frequency ($= \frac{2\pi}{1day}$)

t = Time ($= 10\ days$)

In the physical model experiment that was reproduced in 3DEC, heating and cooling cycles were long enough (approximately three days, Figure 3.15) for the entire model to reach a uniform temperature. Therefore, the sliding block and the wedge are expanding to maximum during each cycle. Shorter period ensures that the temperature distribution within the block will not be uniform, thus allowing differences in the depth of the heat front within blocks, and the sensitivity of the results to different thermal diffusivity can thus be tested. Here the rock mass and the sliding surface are fixed during all simulations, in contrast with the lab validation, where only the velocities parallel to the outward normal to the faces of the block were set to zero. The cumulative displacement, defined by the total displacement of the sliding block after ten days of heating and cooling, is compared for a typical range of the relevant parameters.

As we examine a thermally induced mechanism, we would like to study the effect of the thermal properties of the rock. The effect of the combination of the mechanical and thermal properties on the displacement will be further discussed in section 5.1.

3.5.1 Thermal expansion coefficient

This parameter determines the amount of dilation of the block in response to temperature change. Greater values of thermal expansion coefficient produce greater thermal strains in the rock.

In the model, thermal strain works in both directions. During heating phase, the blocks are expanding, resulting in a dip direction displacement of the sliding block, since the wedge prevents its expansion in the other direction. When the blocks are subjected to decreasing temperature, they contract. The sliding block contracts on both sides,

including some contraction of the sliding block's toe "up the slope". The cumulative displacement after ten days of heating and cooling for typical rock thermal expansion coefficient values is shown in Figure 3.17.

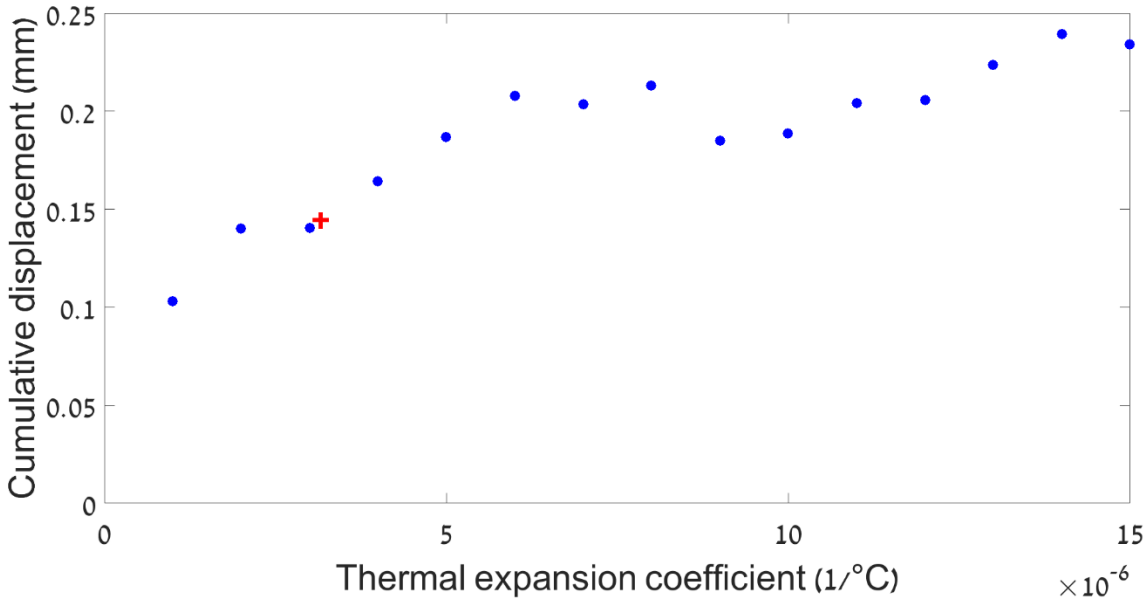

Figure 3.17 – Cumulative displacement as function of the thermal expansion coefficient. Red cross marks the concrete thermal expansion coefficient used for the physical model.

As expected, the cumulative displacement is greater for greater values of thermal expansion coefficient. In each cycle, the sliding block expands more with increasing value of thermal expansion coefficient, consequently leading to greater cumulative displacement. Furthermore, with increasing thermal expansion coefficient the sliding block contracts more during cooling cycles, prompting larger joint opening, and allowing further downward displacement of the wedge. Greater thermal strains lead to greater plastic displacement, even though the thermal strain itself is reversible, due to the wedging mechanism.

3.5.2 Thermal diffusivity

The thermal diffusivity parameter (D_T) determines how fast heat propagates in the medium, defined by:

$$D_T = \frac{k}{\rho * C_p} \tag{39}$$

where:

$k =$ Thermal conductivity ($W/m/K$)

$\rho =$ Bulk density (kg/m^3)

$C_p =$ Specific heat capacity ($J/kg/K$)

In the sensitivity analyses, the thermal diffusivity of the blocks in the model is varied between simulations, in the range of typical rocks. All other parameters remain constant (Table 3).

The minimum thermal time step allowed is inversely proportional to the thermal diffusivity (eq. 30). The time step must be reduced with increasing thermal diffusivity, and therefore cannot be set to the optimal 30 seconds for high values of thermal diffusivity, as determined in the 3DEC sensitivity analysis to numerical control parameters section. For this section only, and for the sole purpose of studying the influence of thermal diffusivity on the displacement, the thermal time step was decreased to 10 seconds in this sensitivity analysis. This way we can prevent the influence of numerical parameters, e.g. the thermal time step, on the displacement as discussed in section 3.4. The mesh size was not changed, and was fixed at an average edge length of 4 cm. The result of this analysis is shown in Figure 3.18.

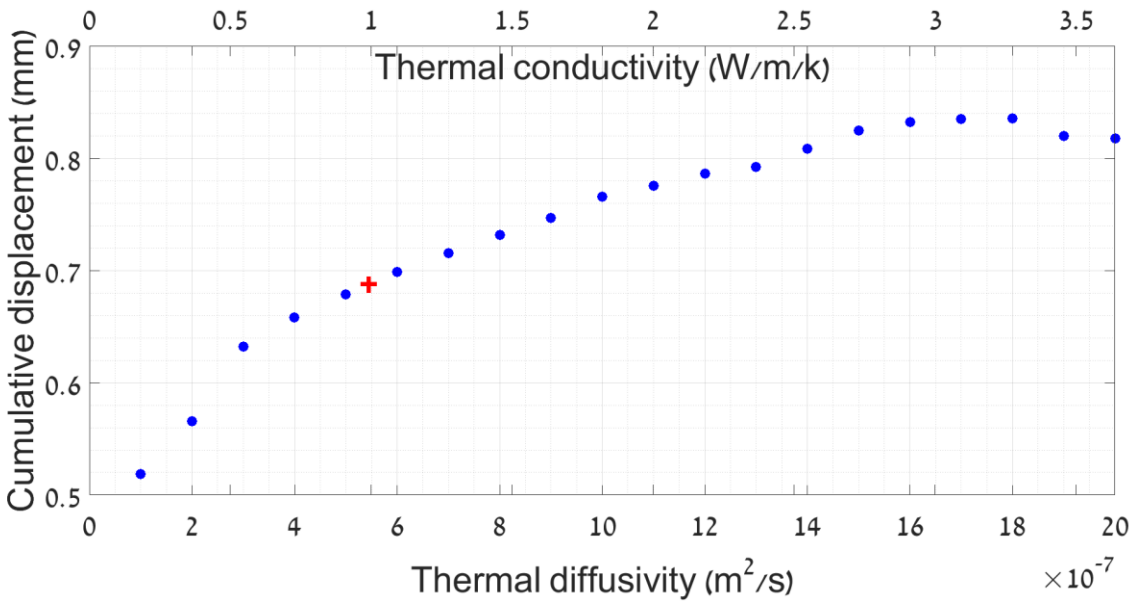

Figure 3.18 - Cumulative displacement, after ten cycles of heating and cooling, as function of thermal diffusivity. Red cross marks the thermal diffusivity of the concrete used for the laboratory experiment.

Heat wave propagates further in the rock with greater diffusivity as is illustrated in Figure 3.19. As more elements within the block are subjected to change in temperature, the block expands more in the model with higher conductivity, and therefore the displacement is expected to be larger. Figure 3.19 presents temperature distribution within blocks when boundary temperature reaches maximum value.

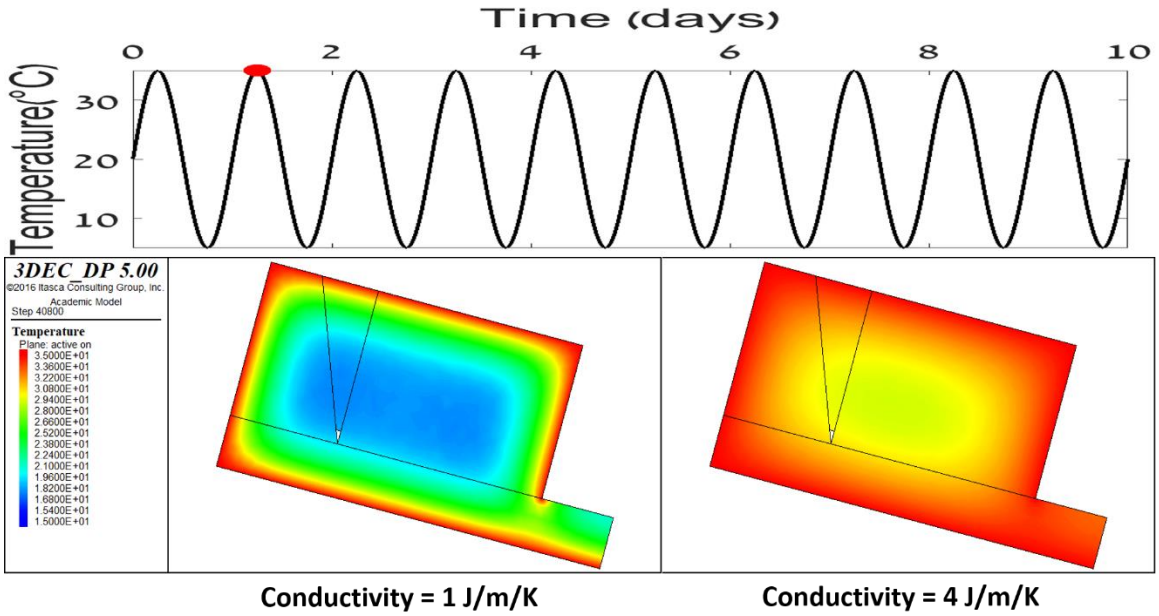

Figure 3.19 – Cross-section of 3DEC model that simulates the physical model (Figure 3.13) with temperature distribution within the blocks in the middle of the second heating cycle, when boundary temperature reaches maximum value (red circle in the upper panel). Heat propagates further in the block with higher thermal conductivity (right panel).

3.5.3 Joint parameters

In this section, we discuss the sensitivity of the numerical model to input joint parameters, specifically the shear stiffness and peak friction angle. Clearly, the frictional resistance to sliding is expected to increase with increasing value of these two interface material parameters.

With increasing shear stiffness, as would be characteristic of rough interfaces with relatively strong asperity material, during application of shear load the joint can absorb more elastic strain that would have been otherwise translated to block displacement. The amount of plastic displacement, therefore, is expected to be much higher under the same remote loading configuration when the shear stiffness is lower, as would be characteristic of smoother surfaces or interfaces with weaker asperity material.

Results of 3DEC simulations of the physical model under a range of joint stiffness values characteristic of rock joint interfaces are presented in Figure 3.20. The modeled cumulative displacement of the sliding block is rather sensitive to the input shear stiffness

value up to shear stiffness of about 1 MPa/mm, beyond which the results are not affected by the stiffness of the interface.

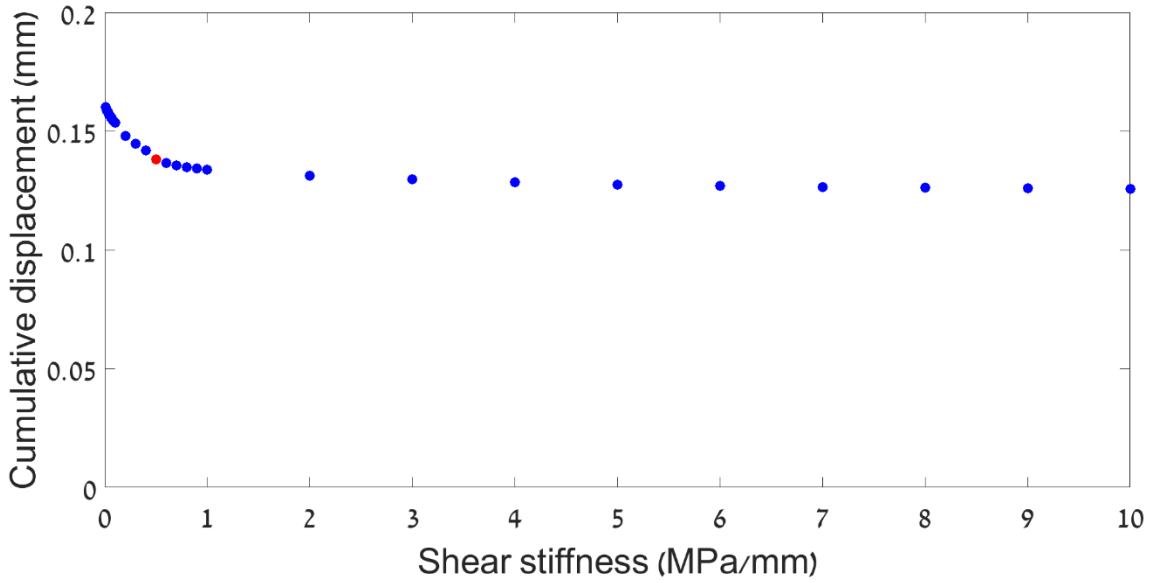

Figure 3.20 – Modeled cumulative displacement as function of the shear stiffness of the joint. Red dot marks the concrete shear stiffness used for the laboratory experiment.

The estimated variance in displacement in the numerical model to input friction angle is intuitively expected. For smaller friction angles, the frictional resistance of the sliding surface is reduced, and the sliding block therefore would be expected to exhibit larger displacement. 3DEC results simulating the physical model for a range of interface friction angles and a joint stiffness value of 0.5 GPa suggest otherwise, however. The results of the simulations (Figure 3.21) reveal that the total cumulative displacement of the block for the tested range of friction angles is not affected very much by the actual value of the input friction angle. Since all values of friction angles tested in the simulations are higher than the inclination of the sliding surface, the obtained displacements are clearly thermally induced. Note also that the friction angle in the numerical model cannot be reduced below 20° even though the interface inclination is 15 degrees, because in reality the wedge applies an additional horizontal force on the sliding block that could prompt a displacement of the sliding block in the numerical model. In the physical model the

available friction angle of the sliding interface was greater than 20 degrees thus arresting this driving mechanism in the laboratory experiment.

The influence of interface friction on the amount of plastic displacement appears to be rather small in the wedging-ratcheting mechanism. Although this result is not immediately intuitive, we can explain it if we consider that thermal expansion and contraction remain the same for any given temperature gradient, regardless of interface friction. The main parameter that drives the thermally induced displacement, the expansion and contraction of the sliding block and of the wedge, remains unchanged, because in contrast to the shear stiffness of the interface, the friction angle cannot absorb the thermally induced elastic displacements.

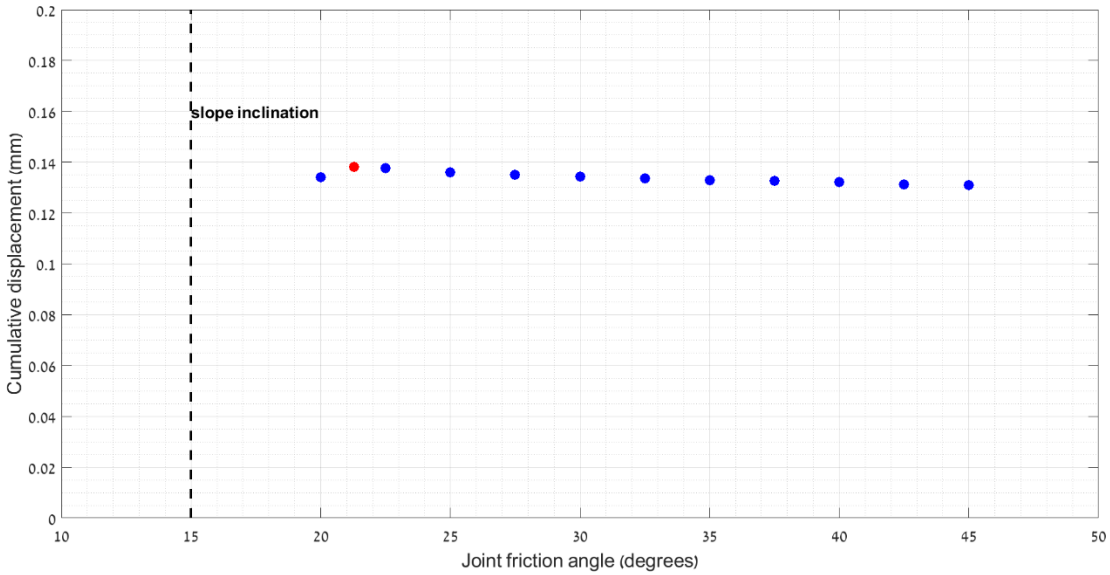

Figure 3.21 - Cumulative displacement as function of joint friction angle. Red dot marks the friction angle of concrete-concrete interface used in the laboratory experiment. Joint stiffness (K_s) was kept constant at 0.5 GPa for all simulations.

Chapter 4 - Application of the wedging-ratcheting mechanism to a field case study

4.1. Introduction

The Masada world heritage site is an old fortress located in the Judean Desert in Israel. It was built on a steep mountain by King Herod the Great more than 2000 years ago. This important monument attracts nearly one million tourists each year. Twenty years ago, during the construction of a new cable car station at the top of the snake path cliff a block displacement was observed, threatening the safety of the workers and the project.

Mount Masada is an uplifted horst located on the western margins of the Dead Sea rift valley. This area is seismically active and experienced many earthquakes in its history (Figure 4.1). The mountain consists mainly of strong carbonate rocks (limestone and dolomite). The rock mass, however, is highly discontinuous and consists of several intersecting joint sets (Hatzor, 2003), creating several removable keyblocks that endanger the designed bridge that connects between the new cable car station and the Snake Path Gate. A particular block, resting directly above the proposed bridge, was marked as hazardous during site investigations in the late 1990's, and an extensive research was thus conducted to investigate potential failure modes, current factor of safety, and alternative support measures. Block displacement was monitored using four different LVDTs that were positioned in various locations between the block and the rock mass for the duration of the construction period.

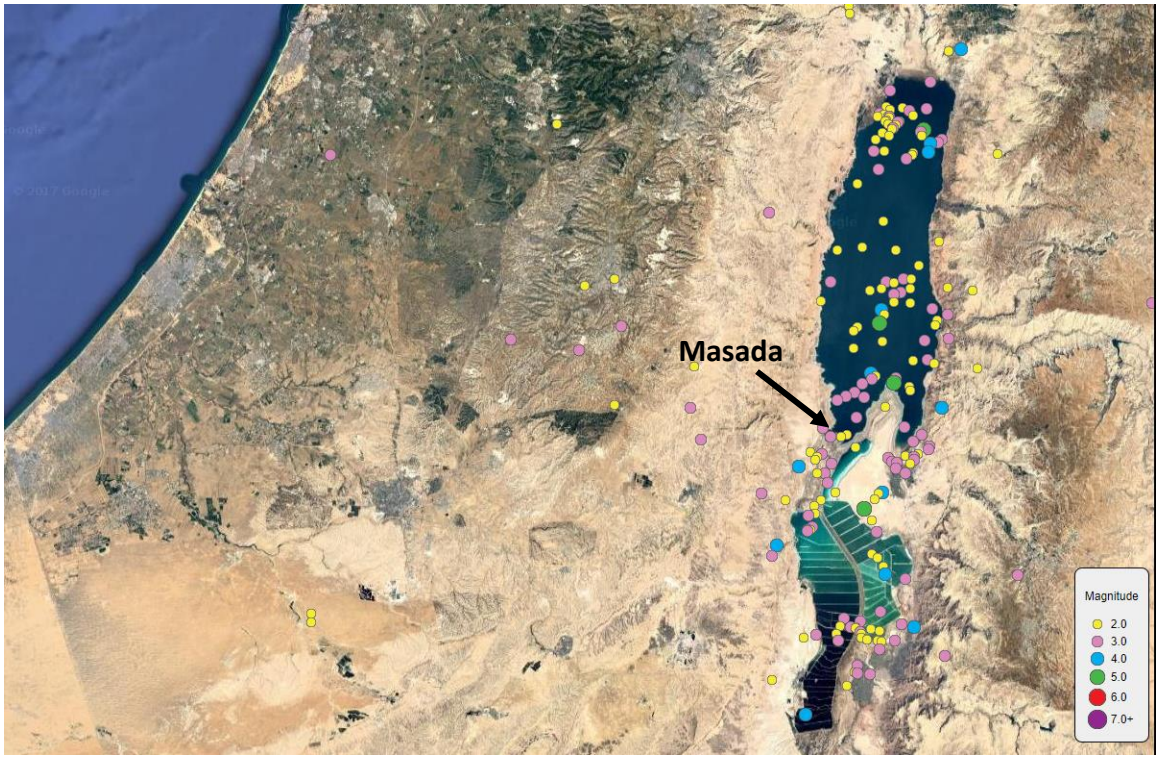

Figure 4.1 - Earthquakes locations since 1950 (The Geophysical Institute of Israel, 2017)

4.2. Geometry and material properties of the removable block

The steep east face of Mount Masada (Snake Path Cliff) is intersected by two orthogonal sets of sub vertical and persistent joints, one striking NNE and the other striking ESE. Spacing between joints in each set is ranging between 5 to 10 meters. Bedding planes are dipping 20° SE. Intersection of members from all three joint sets generate the removable block (Figure 4.2) on which this section is focused (Hatzor, 2003). The study on the East face by Hatzor (2003) of Mount Masada was complemented by Bakun-Mazor et al. (2013) for the West face of Masada. These two studies provide joint displacement monitoring, mechanical and physical parameters of intact rock and discontinuities (Table 4). The geometry of the keyblock in the East face which is used here (Figure 4.3) is adopted from Hatzor (2003).

Figure 4.2 - The removable block and the upper cable car station.

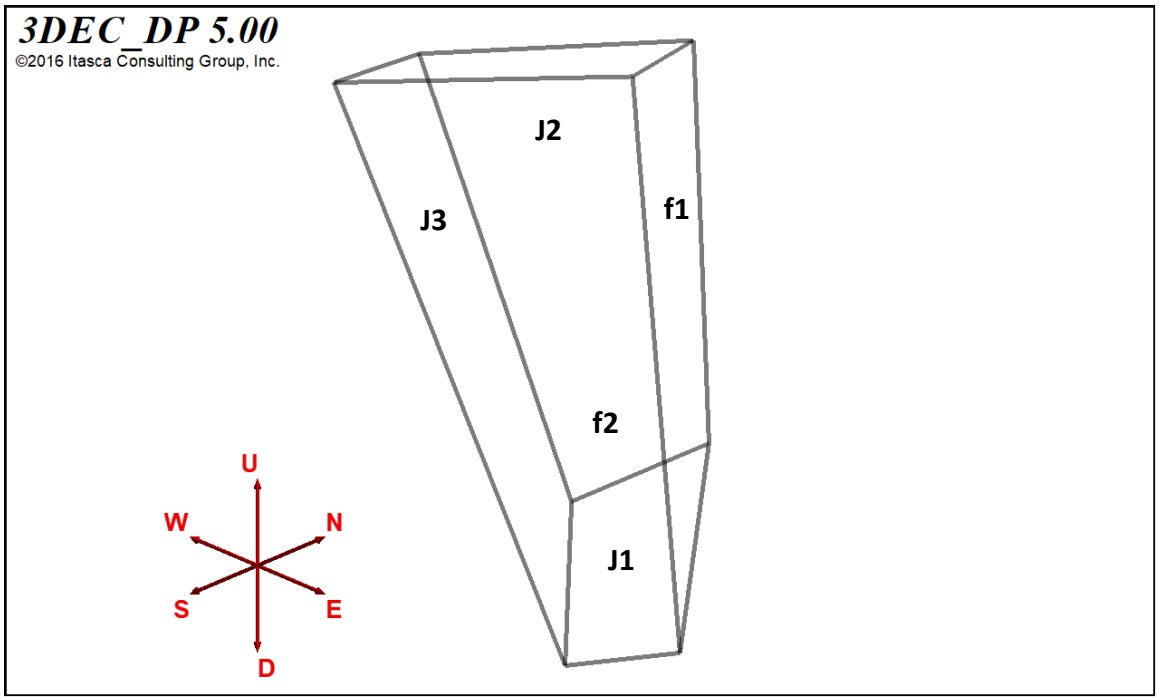

Figure 4.3 - Block geometry. Faces (f_i) and joints (j_i) are marked on the surfaces.

Table 4 - Properties of the removable block in Masada.

	Parameter	*Symbol*	*Units*	*Value*	*Source*
Block geometry	Bedding plane	J_1	dip/dip direction	20/124	Hatzor (2003)
	Joint 2	J_2	-	84/107	
	Joint 3	J_3	-	75/052	
	Face surface 1	f_1	-	84/060	
	Face surface 2	f_2	-	90/126	
	Block volume	V	m^3	563	
Material properties	Elastic modulus	E	GPa	40	Bakun-Mazor et al. (2013)
	Poisson's ratio	ν	-	0.2	
	Bulk density	ρ	Kg/m^3	2600	
	Block weight	W	10^6kg	1.465	
Joints properties	Peak friction angle	ϕ_p	°	41	Hatzor (2003)
	Saw-cut friction angle	ϕ_{saw}	°	28	
	Residual friction angle	ϕ_{res}	°	23	
	Normal stiffness	K_n	GPa/m	5	Bakun-Mazor et al. (2013)
	Shear stiffness	K_s	GPa/m	1	
Thermal properties	Thermal expansion coefficient	α	10^{-6}/°C	6-8	Bakun-Mazor et al. (2013)
	Thermal conductivity	λ	W/m/k	1.7	
	Specific heat capacity	C_p	J/kg/K	810	Rohsenow et al. (1998)

The studied block is massive with height of 15 meters and width of about 10 meters. It is resting on a moderately dipping bedding plane and is separated from the rock mass by two sub vertical joints. Across Joint no. 2 (a member of joint set 2) there is a displacement of 20 - 40 cm (Figure 4.4) that has accumulated over its geological history. The tension crack is filled with rock fragments with various sizes in its upper part, and with softer rock and soil at the bottom.

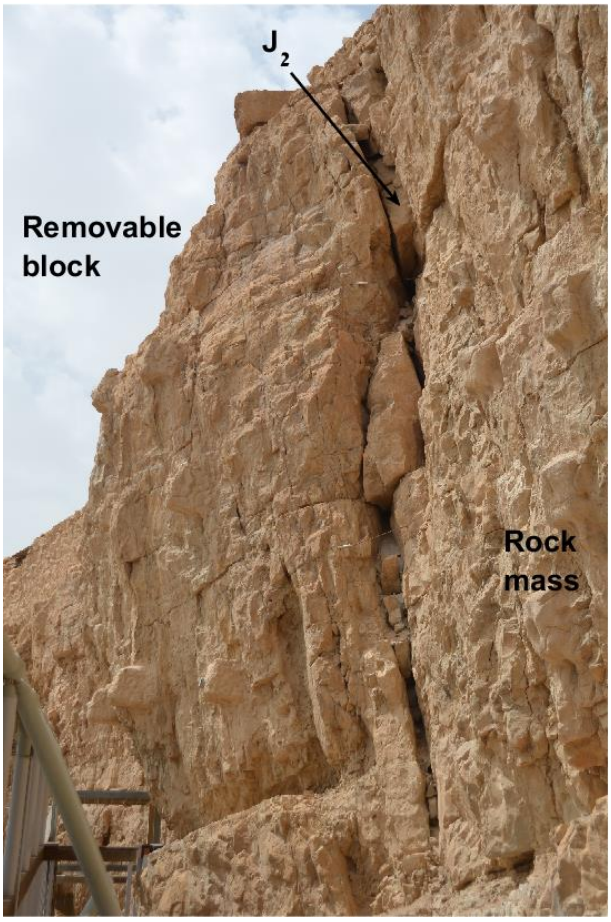

Figure 4.4 - The removable block and the opened joint J2.

Joint no. 3 (a member of joint set 3) that separates the block from the rock mass is tightly closed (Figure 4.5), and it appears that no opening occurred across it over its geological history.

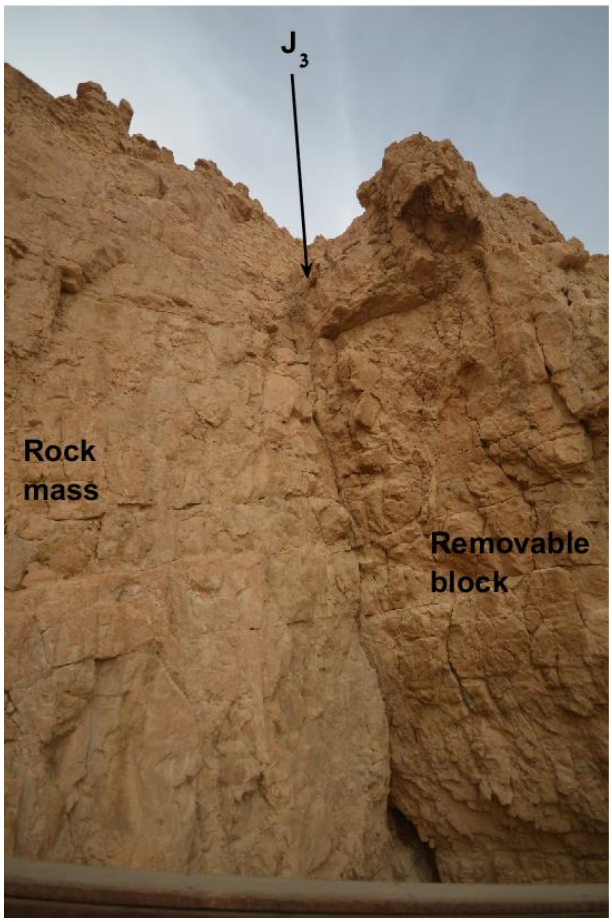

Figure 4.5 - The removable block and the closed joint J3.

Four joint meters (LVDT) were installed on both joints to measure relative displacement between the rock mass and the removable block (Figure 4.6). Joint meters were mounted in direction normal to the joints and measured joint opening and closure. The LVDTs were active from January to November 1998, when the block (and many others) was anchored to the rock mass with cable bolts. The block displacement, therefore, was monitored for only half of a complete thermal cycle.

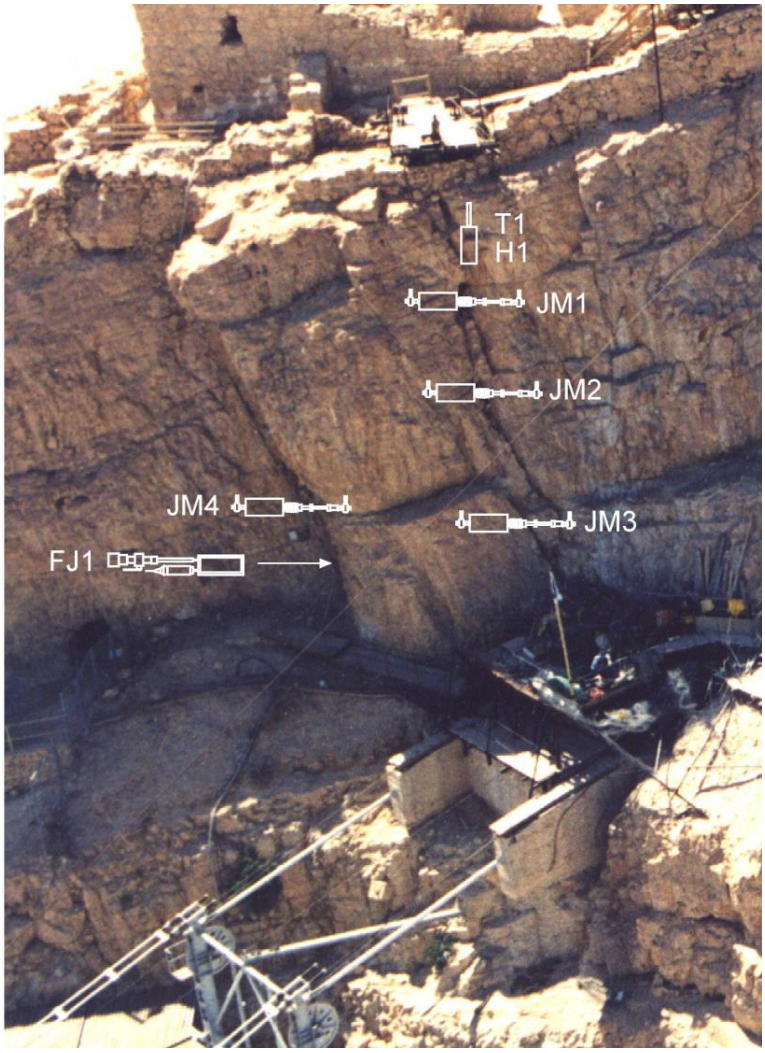

Figure 4.6 - "Block 1" and the configuration of the joint meters (Hatzor, 2003)

In April 1998, there was a sudden increase in temperature (Figure 4.9), followed by an abrupt displacement across the joints, as inferred from the output of the four joint meters. During this heating cycle it is reasonable to assume that the removable block expanded in all directions, including upwards, resulting in boundary - joints closure. Comes August, temperature gradually decreases, followed by thermal contraction of the removable block, resulting in a progressively opening of the joint (J2), as nicely depicted by the output of joint meter 3 (see Figure 4.7).

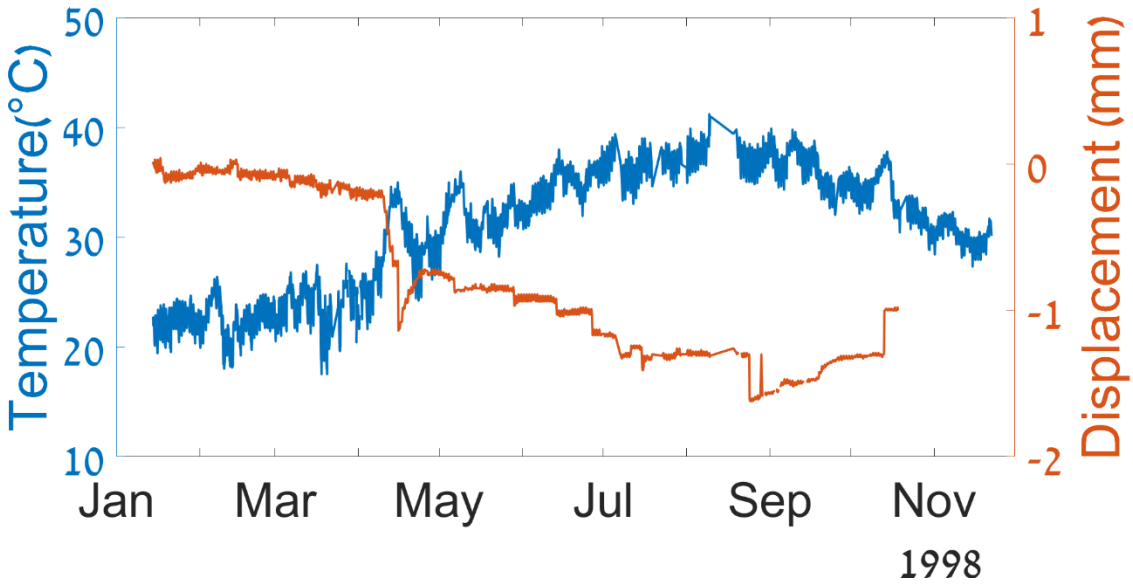

Figure 4.7 - Displacement of the "Block 1" in the east face of Masada cliff, as recorded by JM3 (Hatzor, 2003). Sudden increase in Temperature (blue line) is followed by ~1 mm displacement (red line).

4.3. 3DEC model

The geometry of the block and its surrounding were reproduced in 3DEC using the data from Table 4. Two friction angles were chosen to represent the sliding surface, peak and saw-cut values (the residual friction angle is slightly lower – see Table 4). The saw-cut friction angle is also considered in the analysis in addition to the peak value on account for the fact that the block has displaced in its past and the assumption that the sliding surface has deteriorated somewhat in the course of this historic displacements. For simplicity, the filling material inside the tension crack $J2$ (Figure 4.4) is modeled here as a single prismatic wedge, occupying the full width of the crack, and its upper two thirds of height (Figure 4.8). The rock mass is fixed (no velocity in all directions) for the entire simulation, whereas the removable block (referred to as "Block 1" following Hatzor, 2003 notation) and the wedge are free to move. The initial temperature of the blocks is assumed uniform.

Blocks are discretized using a uniform mesh with an average tetrahedron edge length of 30 cm, which is about 5% of the sliding block length in the direction of sliding, as per the optimized ratio obtained in section 3.4. Since the scale of this model is much larger than

the physical model tested in the previous chapter, the explicit thermal time step is larger and is set to 400 seconds (see simulation code in Appendix E). The temperature log obtained by Hatzor (2003) is partial and does not comprise of a complete cycle of heating and cooling because the block was reinforced with cable bolts in the middle of one thermal cycle. After initial equilibrium is obtained in the model (as in section 3.3), the temperature history obtained through three consecutive years, between 2012 and 2015, measured by the Israel Meteorological Service (2017) in Ein-Gedi station (15 km from Mount Masada), was applied to the outer boundaries of the blocks, to simulate the response of the system to a full cycle of heating and cooling.

This 3DEC model is less sensitive to changes in time step, compared to the reproduction of the physical model in section 3.4, since the block is much bigger and less sensitive to short periods of temperature changes; thus, the model remains in mechanical equilibrium. To avoid displacement artifacts resulting from immediate response due to thermal expansion of the boundaries, or elastic displacement of joint asperities via the input shear stiffness, the displacement of the center of mass of “block 1” was recorded and stored for further analysis. Note that field measurements performed with joint meters are not equivalent to the displacement recorded in 3DEC simulation, as the exact orientation of the LVDT’s is unknown.

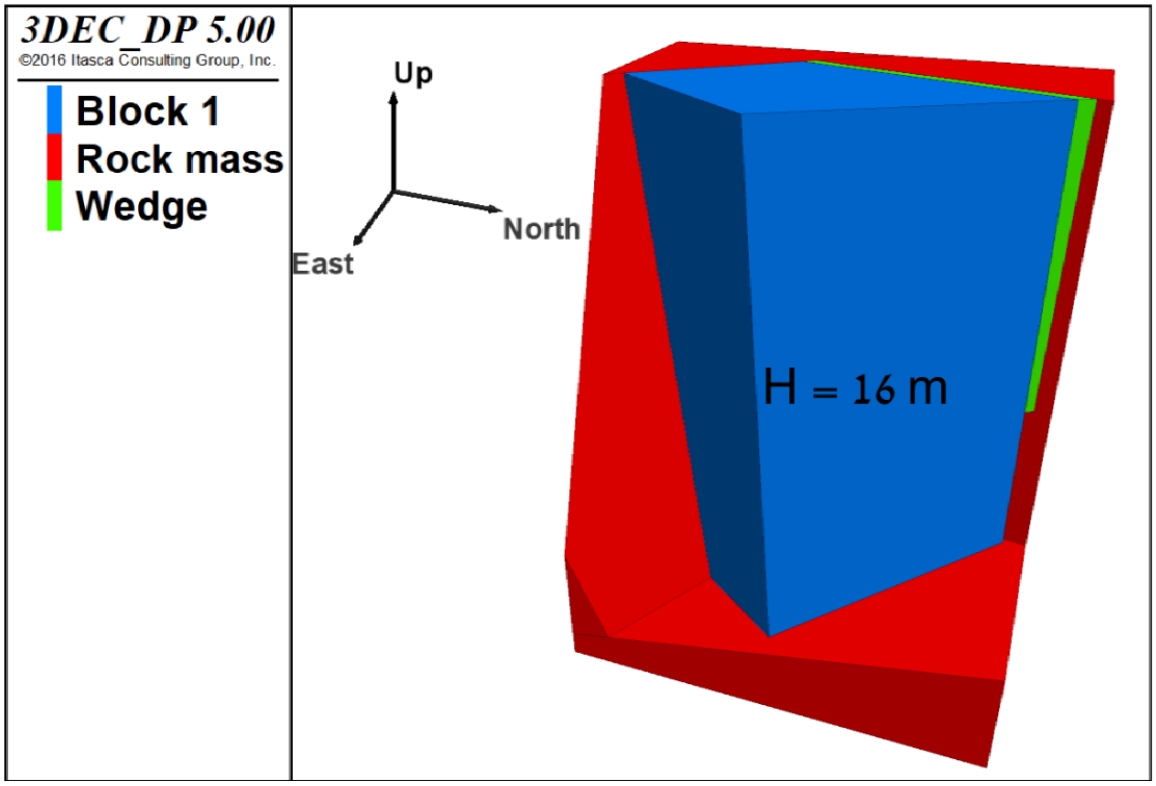

Figure 4.8 – Masada 3DEC model.

The results of the 3DEC simulations are shown in Figure 4.9. The displacement of the block occurs mostly during the heating phases. During that time, the block expands, compressive stresses develop around the wedge, and the position of the wedge in the joint prompts displacement of the block down the sliding surface (Figure 4.10). The cumulative displacement over the three years is between 0.7 to 1.3 mm depending on the assumed value of frictional resistance across the sliding plane. Thus, the expected annual displacement is 0.24-0.44 mm per year, depending on the exact value of the friction angle.

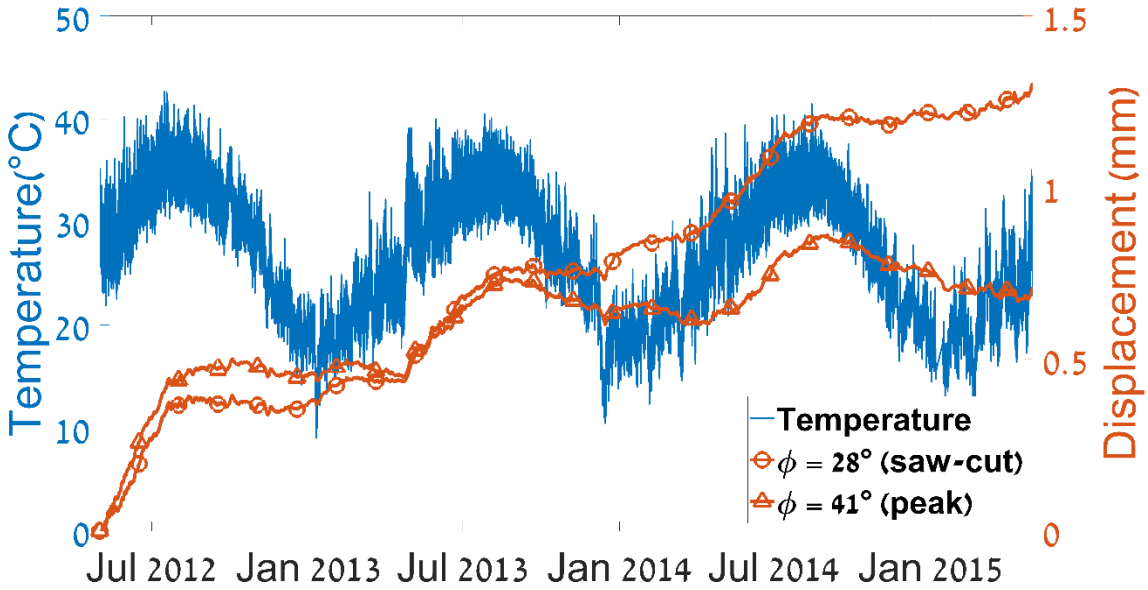

Figure 4.9 - Masada 3DEC model displacement for two friction angles, saw-cut (red dotted line) and peak (red continuous line). Temperature applied to block boundaries is in blue.

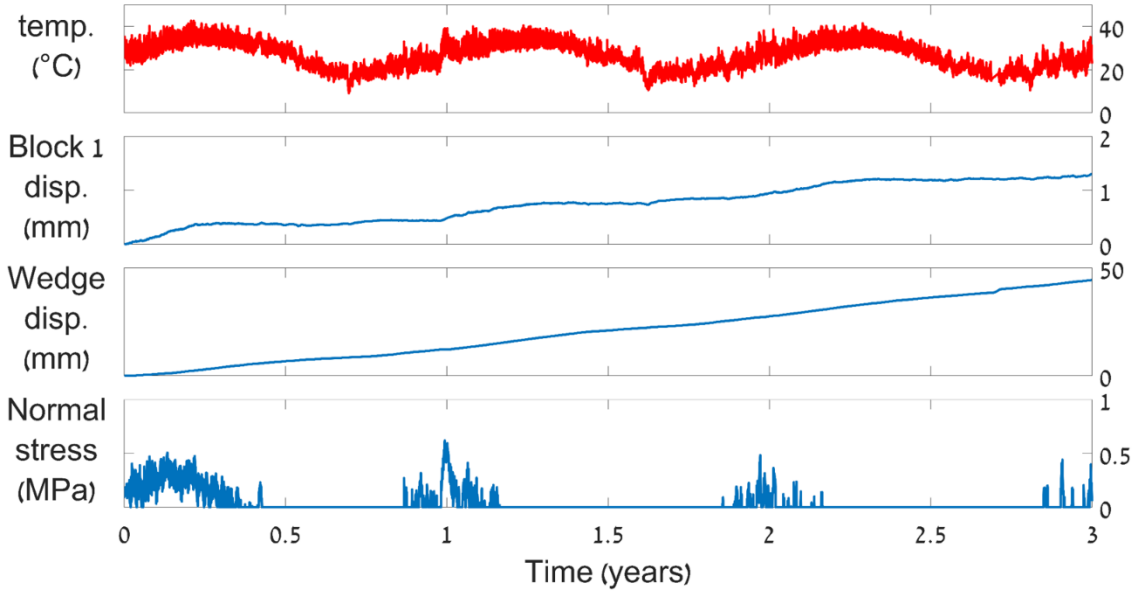

Figure 4.10 – 3DEC model displacement of "Block 1" ($\phi = 28°$). (a) Temperature applied to block boundaries. (b) "Block 1" center of mass displacement. (c) Wedge displacement down the opening joint. (d) Compressive normal stress at the back of the wedge.

Chapter 5 - Discussion

Numerical simulations of the wedging-ratcheting mechanism reveal the possible outcomes of a thermally induced failure mechanism in jointed rock slopes. The results in this research show that given certain conditions, such as the geometry of the problem, thermomechanical properties, and temperature oscillations magnitude, the wedging-ratcheting mechanism can explain small annual displacements. A large-scale physical model, conducted in a climatically controlled room, supports these findings.

This section provides further analysis to the previous sections, and presents a comparison of the results with other failure mechanisms.

5.1. Rock types prone to wedging-ratcheting failure mechanism

The magnitude of the displacement due to temperature fluctuations is dependent on rock and joint properties, as described in section 3.5. Below a brief comparative study is conducted to determine which rock types are more likely to exhibit thermally induced displacements. For that purpose, we use the 3DEC model that reproduces the physical model (section 3.3), since it was validated with experimental data, and because it is simpler and requires less computational resources.

Rocks, even if are members of the same group (e.g. sedimentary or igneous), differ in their thermal properties, since the mineralogy varies significantly among the rock types. For instance, Schütz et al. (2012) studied the thermal conductivity of sedimentary rocks in Israel. For each formation examined in their study, the thermal conductivity range was found to be relatively wide. For the comparative examination in this study, a single value is assumed for each of the thermal and mechanical properties to represent its group (Table 5).

Table 5 – Typical thermomechanical properties of some rocks.

Parameter	***Symbol***	***Units***	***Granite***	***Basalt***	***Sandstone***	***Dolomite***
Elastic modulus	E	GPa	50[(1)]	70[(1)]	20[(9)]	48[(12)]
Poisson's ratio	ν	-	0.2[(2)]	0.28[(2)]	0.25[(10)]	0.26[(12)]
Bulk density	ρ	Kg/m^3	2650[(1)]	2870[(5)]	2640[(5)]	2550[(12)]
Thermal expansion coefficient	α	10^{-6}/°C	8[(3)]	5[(6)]	11[(11)]	8[(3)]
Thermal conductivity	k	W/m/K	2.5[(4)]	1.2[(7)]	3.3[(6)]	4.5[(6)]
Specific heat capacity	C_p	J/kg/K	840[(4)]	840[(8)]	900[(8)]	900[(8)]
Thermal diffusivity (calculated)	κ	10^{-6}m^2/sec	1.12	0.50	1.39	1.96

References: (1) Turcotte and Schubert (2014); (2) Vutukuri et al. (1974); (3) Franklin and Dusseault (1991) ENREF 20*; (4) Heuze (1983); (5) Jaeger et al. (2009); (6) Naeser et al. (1989); (7) Blesch et al. (1983); (8) Eppelbaum et al. (2014); (9) Vásárhelyi (2003); (10) Gercek (2007); (11) Engineering Toolbox (2017); (12) Hatzor and Palchik (1997).*

The geometry of the model and the applied temperature remained constant for all simulations. Since it was observed earlier in this research that friction angle does not play a significant role in the mechanism, the same value of friction angle (32°) applied to the joints in all simulations. Shear and normal stiffness of the joint were kept constant, and set to 1 and 5 GPa/m, respectively. The boundaries of the model were subjected to a sinusoidal input temperature with a period of one day for three days (three cycles of heating and cooling, red line in Figure 5.1). The exposure time was not long enough for the block to reach uniform temperature even in the model with the greatest thermal conductivity. The upper panel in Figure 5.1 presents the temperature log of the center of mass of the sliding block and it shows the difference in heat propagation within blocks in simulations with different thermal conductivity input. The displacement of the center of mass of the sliding block down the inclined plane was recorded and the results are plotted in the lower panel of Figure 5.1.

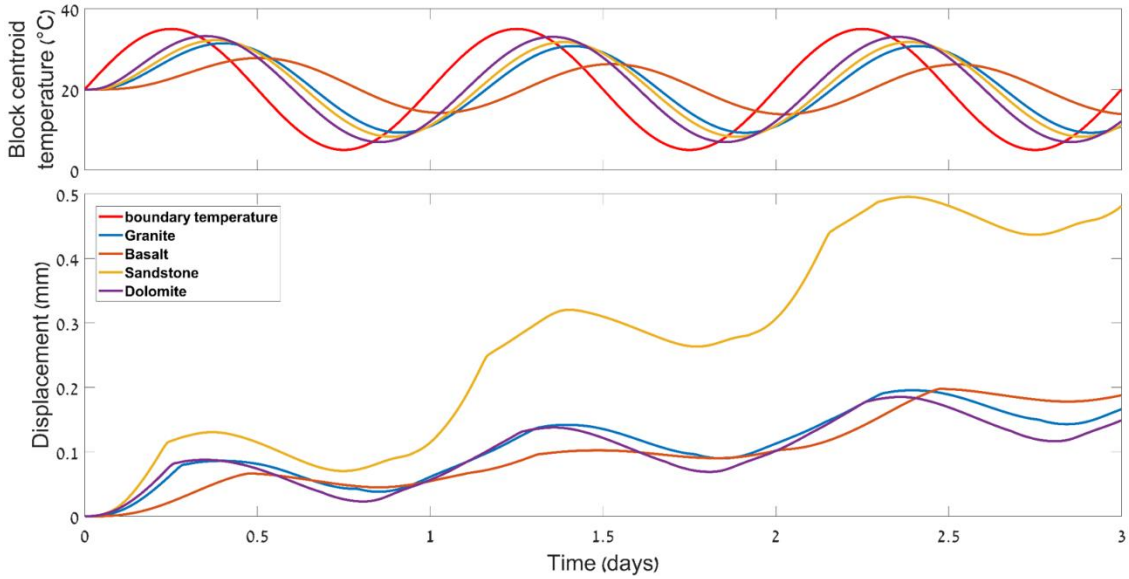

Figure 5.1 - Displacement of the sliding block in the dip direction (lower plot). The center of the sliding block does not reach the temperature applied to the boundaries (red curve in the upper plot).

It can be inferred from the results that the most significant parameter in the displacement is the thermal expansion coefficient of the block material. Of the rock types studied, indeed the sandstone appears to be the most sensitive to the wedging-ratcheting mechanism, since its thermal expansion coefficient is the greatest, even though its thermal conductivity is significantly lower than the dolomite. Surprisingly, the displacement exhibited by the dolomite is almost equal to the displacement exhibited by the basalt, even though the dolomite's thermal conductivity is much greater. The different densities of both rocks can explain this. The density of the basalt is greater, so the wedge is heavier and applies greater force on the sliding block. That way, under gravity only, the basalt's sliding block is closer to equilibrium state, and less thermal expansion is needed to achieve plastic displacement. The mechanical properties, therefore, are also playing a role in the thermally induced mechanism.

5.2. Case study – removable block on Mount Masada

5.2.1 Annual displacement of "Block 1", Masada

The displacement of "Block 1" in Masada, as obtained with field measurements (4.2) and with 3DEC simulations (4.3), is rather minor, and for sustainability of engineering structures with a design life time of 50 – 100 years may be considered negligible. For natural rock slopes, however, this rate may lead to significant displacements over geological time scales that can advance the deterioration rate of the rock mass. We therefore wish to understand the cumulative nature of the wedging-ratcheting mechanism over long periods.

The removable block slides down the slope, according to 3DEC analysis in section 4.3, at a rate of 0.24-0.44 millimeters per year, depending on the assumed frictional resistance across the sliding surface. The most important feature presented in Figure 4.9, however, is the irreversible nature of this displacement. In each phase of displacement, the wedge slides further down the opening joint, preventing block displacement back up the slope; once the wedge takes its place in the joint, it cannot move up, only down. Since the displacement is irreversible, the small magnitude of annual displacement and its slow rate is of no significance; the displacement can accumulate over years and decades, assuming the opening joint is continuously filled with new rock fragments.

As predicted by the wedging-ratcheting mechanism, most of the displacement occurs when the temperature is rising (transition from winter to summer). However, some displacement can be observed during winter, due to short period of heating (for example the third shaded area from the left in Figure 5.2). This can be associated with displacement mode introduced by Taboada et al. (2017) described in section 1.1, in which short-term thermal cycles of between 2 to 15 days can cause thermally induced displacements.

It is important to determine whether daily temperature fluctuations play a significant role in the total accumulated displacement. For this purpose the real temperature input record used in the 3DEC simulation described in 4.3 is now represented by a fitted

sinusoidal function (red line in the upper panel of Figure 5.2) to eliminate the short-term temperature changes, and the system response is reanalyzed.

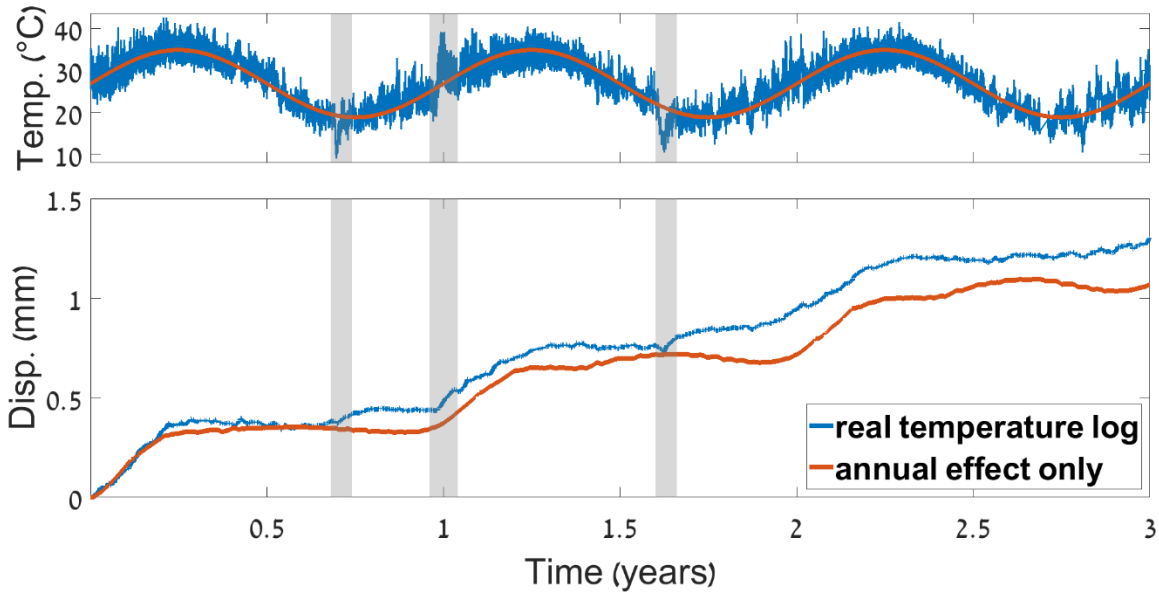

Figure 5.2 - Comparison between annual and daily temperature fluctuations. Temperature input for the simulations in the upper plot, displacement for each simulation in the lower plot.

We find that displacements obtained in both 3DEC simulations are essentially the same, and it can be concluded, therefore, that daily temperature fluctuations do not play a significant role in the overall mechanism. Heat does not propagate deep enough in the rock in short exposure periods to cause significant expansion or contraction. However, the role of high frequency changes (daily temperature fluctuations) can be more significant in smaller blocks or rocks with greater thermal conductivity, as a larger portion of the block will be influenced by the temperature changes. The slight change in displacement between both simulations is maybe due to short periods of dramatic temperature change that are delineated as shaded areas in Figure 5.2. Such an effect can explain the relatively large displacement of ~1 mm measured by Hatzor (2003) during the 5 months of monitoring in the field in 1998 (see Figure 4.7).

5.2.2 Comparison with other proposed models

Thermal mechanisms

Part of the accumulated displacement of the sliding block down the sliding interface is due to the so called "crawling motion" suggested by Gunzburger et al. (2005) and introduced in section 1.1. We want to compare the degree of influence of each mechanism ("crawling motion" vs. wedging-ratcheting) on the cumulative displacement of the block.

The same block model from the snake path cliff in Masada (Figure 4.8) is used for this test. Two block configurations are simulated, one with a wedge in the tension crack and another without the wedge, the latter in order to represent a simple problem of a block on an inclined plane subjected to temperature oscillations. The 3DEC model used for this analysis is shown in Figure 5.3.

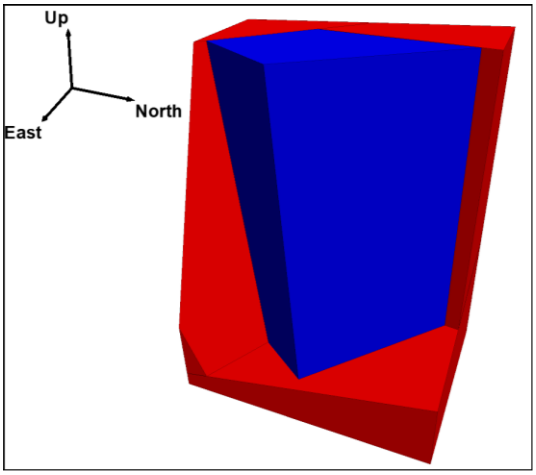

Figure 5.3 – Masada 3DEC model with no wedge in the joint. This model was used to examine the amount of the "crawling motion" displacement.

A three-year temperature log was applied on the boundaries in both models (with and without a wedge in the tension crack). To avoid the influence of dramatic temperature changes that occur over short periods during a cycle, we use here a smoothed temperature history, represented by a sinusoidal function. The input temperature history and the response of the two geometrical configurations as modeled with 3DEC is shown in Figure 5.4.

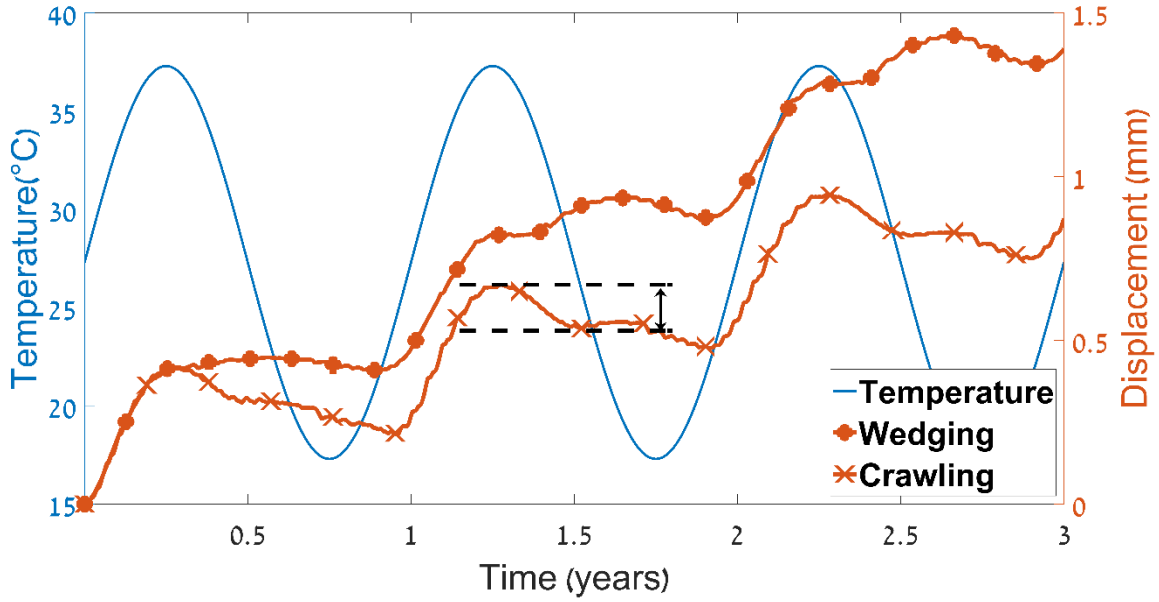

Figure 5.4 - Comparison of two different thermally induced failure mechanisms, the "crawling motion", suggested by Gunzburger (red line with x symbols), and the wedging-ratcheting mechanism (red line with circles). Note the reversible displacement during cooling phases, marked by black lines. Since there is no wedge in the joint, during that time, the block contracts in all directions, including contraction up the slope.

The results plotted in Figure 5.4 reveal that the displacement due to the wedging-ratcheting mechanism is almost twice as much as due to the "crawling motion" when everything else is kept equal. Moreover, we can infer from the results that the self-weight of the wedge is not the reason for the difference in displacement between the two mechanisms. For each heating phase, when most of the displacement takes place, the amount of displacement for the two mechanisms is essentially the same. The difference between the two mechanisms, therefore, can be explained by the mere presence of the wedge in the joint, preventing contraction of the block's toe of the sliding block "up the slope". In the model without the wedge, during cooling phases, the block slides a little bit back up the slope, as there is no wedge to preclude such displacement. Thus, the wedging-ratcheting mechanism has a considerable addition to the "crawling motion" mechanism.

Seismic triggering

The location of Mount Masada near an active fault calls for the consideration of a seismically induced displacement. studied the response of the modeled block in this

thesis, “Block 1” in Masada, to dynamic loading using the numerical, discrete element Discontinuous Deformation Analysis (DDA) method (Shi, 1993).

Using an input motion based on the 1995 Nuweiba earthquake (for details see Hatzor, 2004), the researchers determined numerically the expected displacement of Block 1 that would have been caused by earthquake sources in the Dead Sea Transform, 1 km from Mount Masada, and their results for events of magnitude 6 to 7.5 are presented in Figure 5.5. Note that the results shown in Figure 5.5 are the expected accumulated displacement of Block 1 during a single event based on the input motion that includes the topographic effect of Masada, for an earthquake source at a distance of 1 km from the site.

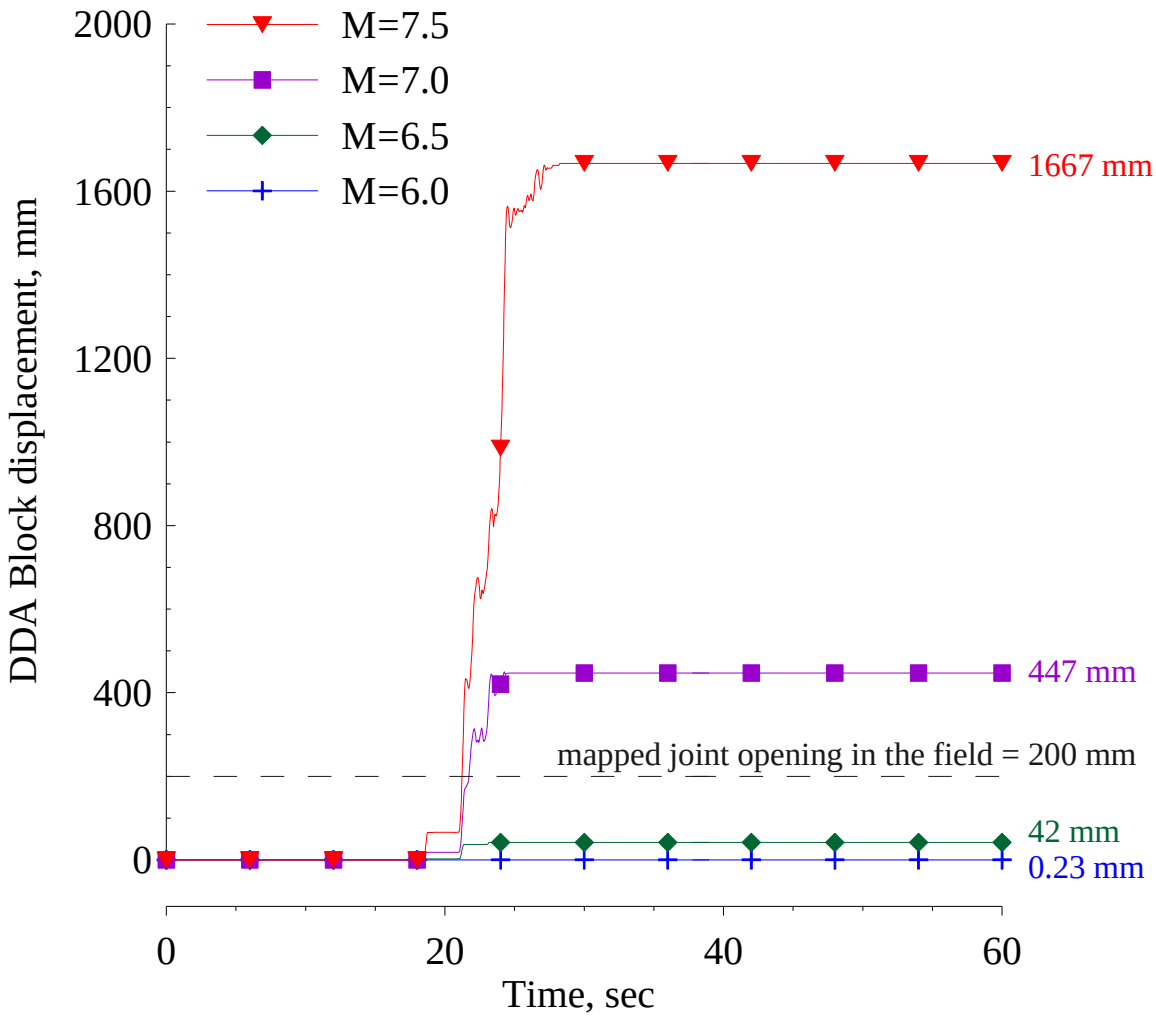

Figure 5.5 – The expected displacement of "Block 1" when subjected to a dynamic loading of four different earthquake magnitudes (Bakun-Mazor et al., 2013).

The recurrence of moderate (M_w=6.5) and strong (M_w=7) earthquakes was assumed to be 1100 and 4000 years, respectively, based on the local seismicity of the region (Begin, 2005, and Shapira et al., 2007). The expected total accumulated displacement in a 5000 years window can therefore be compared for both seismic and thermally induced mechanisms. Figure 5.6 presents a comparison of the expected seismic displacement obtained by Bakun-Mazor et al. (2013) and the expected thermally induced displacement found in this study based on the 3DEC model, namely 0.24 mm/year assuming a continuous supply of rock fragments filling the increased aperture and the lower bound of available friction across the sliding interface. It is important to point out that the slip

rate can change over such a long period of time, as the wedge volume is increasing, and the frictional resistance of the sliding surface can deteriorate over time.

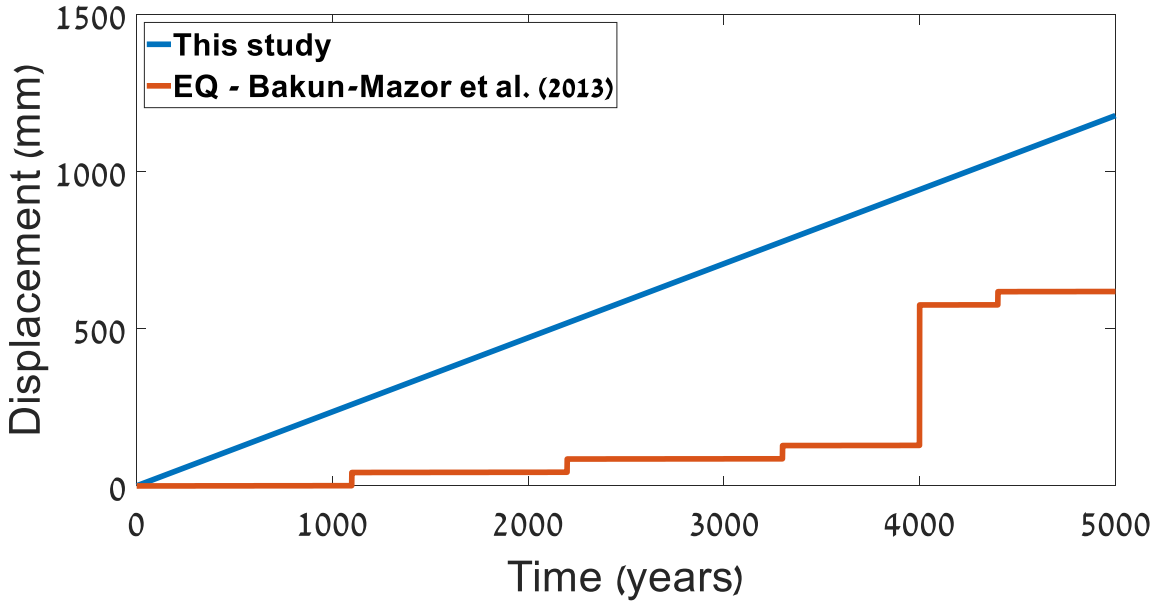

Figure 5.6 – A comparison between two different failure mechanisms, thermally induced wedging-ratcheting (blue) and seismic triggering (red), if each mechanism works independently.

The total displacement of "Block 1" due to temperature oscillations for the case of Masada is greater than the seismically induced displacement when everything else is equal. The cumulative nature of the wedging-ratcheting mechanism makes the thermally induced displacement significant in terms of long-term geomorphology, even when comparing with seismic triggering, in an area considered seismically active, such as the Dead-Sea Transform. Therefore, the wedging-ratcheting mechanism has an important role in shaping the landscape, and is indeed a failure mode that cannot be ignored when considering rock slope instabilities in the long term.

Chapter 6 - Conclusions

The objective of this research was to examine the feasibility of the thermally induced wedging-ratcheting mechanism using the numerical distinct element method in three dimensions (3DEC). First, we validated the numerical results with laboratory experiments. Later, we studied a case study from Mount Masada, Israel.

We obtained the following results:

1. Thermally induced wedging-ratcheting mechanism is proved to cause irreversible displacement down an inclined slope. Heating phases are linked with dilation of the blocks in the system, resulting in compressive stress evolution around the joints, prompting block displacement down the sliding interface. Cooling phases are associated with contraction, resulting in joint opening and further sliding of the wedge down the aperture of the tension crack behind the sliding block.
2. The numerical 3DEC platform used in this research is proved valid for the purposes of this study. Some issues that require further investigation have been explored, including the sensitivity of the results to the choice of numerical control parameters such as time step size and element size. Therefore, the verification and validation stages in the research were necessary for the calibration of the numerical control parameters, and consequently to produce reliable results.
3. Some lithologies are more prone to thermally induced displacement, mainly due to their higher thermal expansion coefficient. This is because the primary factor that drives the mechanism forward is thermal expansion and contraction of the rock, both the wedge and the sliding block.
4. The infinite possible configurations of the blocks system and properties makes an analytical solution that is not over-simplified hard to obtain. However, a comprehensive study of the configuration and geometry of a problem in the field, accompanied by laboratory tests and experiments to determine the thermo-mechanical properties of the rock, can lead to an educated simulation that produces a reliable result.

5. The irreversible and cumulative nature of the displacement (on account of the wedge driving the mechanism in one direction) has an addition contribution to the total displacement of the block, compared with other known mechanisms, thermally or seismic induced (e.g. the “crawling motion” and earthquakes).
6. The proposed failure mechanism may play a significant role in slope stability problems due to the cumulative and repetitive nature of the displacement.

Bibliography

BAKUN-MAZOR, D., HATZOR, Y. H., GLASER, S. D. & SANTAMARINA, C. J. 2013. Thermally vs. seismically induced block displacements in Masada rock slopes. *International Journal of Rock Mechanics and Mining Sciences,* 61**,** 196-211.

BEGIN, Z. E. B. 2005. *Destructive Earthquakes in the Jordan Valley and the Dead Sea: Their Recurrence Intervals and the Probability of Their Occurrence*, Geological Survey of Israel.

BLESCH, C., KULACKI, F. & CHRISTENSEN, R. 1983. Application of integral methods to prediction of heat transfer from a nuclear waste repository. Ohio State Univ. Research Foundation, Columbus (USA).

CARSLAW, H. & JAEGER, J. 1959. *Heat in solids*, Clarendon Press, Oxford.

COLLINS, B. D. & STOCK, G. M. 2016. Rockfall triggering by cyclic thermal stressing of exfoliation fractures. *Nature Geoscience,* 9**,** 395-400.

CUNDALL, P. A. Formulation of a three-dimensional distinct element model—Part I. A scheme to detect and represent contacts in a system composed of many polyhedral blocks. International Journal of Rock Mechanics and Mining Sciences & Geomechanics Abstracts, 1988. Elsevier, 107-116.

CUNDALL, P. A. & HART, R. D. 1992. Numerical modelling of discontinua. *Engineering computations,* 9**,** 101-113.

ENGINEERING TOOLBOX. 2017. *Coefficients of Linear Thermal Expansion* [Online]. [Accessed].

EPPELBAUM, L., KUTASOV, I. & PILCHIN, A. 2014. Thermal properties of rocks and density of fluids. *Applied geothermics.* Springer.

FELDHEIM, A. 2017. *Experimental study of thermally induced wedging-ratcheting mechanism in rock slopes.* M.Sc, Ben-Gurion University of the Negev.

FRANKLIN, J. A. & DUSSEAULT, M. B. 1991. Rock engineering applications, 1991.

GERCEK, H. 2007. Poisson's ratio values for rocks. *International Journal of Rock Mechanics and Mining Sciences,* 44**,** 1-13.

GISCHIG, V. S., MOORE, J. R., EVANS, K. F., AMANN, F. & LOEW, S. 2011. Thermomechanical forcing of deep rock slope deformation: 1. Conceptual study of a simplified slope. *Journal of Geophysical Research,* 116.

GREIF, V., SIMKOVA, I. & VLCKO, J. 2014. Physical model of the mechanism for thermal wedging failure in rocks. *Landslide science for a safer geoenvironment.* Springer.

GUNZBURGER, Y., MERRIEN-SOUKATCHOFF, V. & GUGLIELMI, Y. 2005. Influence of daily surface temperature fluctuations on rock slope stability: case study of the Rochers de Valabres slope (France). *International Journal of Rock Mechanics and Mining Sciences,* 42**,** 331-349.

HART, R., CUNDALL, P. & LEMOS, J. Formulation of a three-dimensional distinct element model—Part II. Mechanical calculations for motion and interaction of a system composed of many polyhedral blocks. International Journal of Rock Mechanics and Mining Sciences & Geomechanics Abstracts, 1988. Elsevier, 117-125.

HATZOR, Y., ARZI, A., ZASLAVSKY, Y. & SHAPIRA, A. 2004. Dynamic stability analysis of jointed rock slopes using the DDA method: King Herod's Palace, Masada, Israel. *International Journal of Rock Mechanics and Mining Sciences,* 41**,** 813-832.

HATZOR, Y. H. 2003. Keyblock stability in seismically active rock slopes—Snake Path cliff, Masada. *Journal of geotechnical and geoenvironmental engineering,* 129**,** 697-710.

HATZOR, Y. H. & PALCHIK, V. 1997. The influence of grain size and porosity on crack initiation stress and critical flaw length in dolomites. *International Journal of Rock Mechanics and Mining Sciences,* 34**,** 805-816.

HEUZE, F. High-temperature mechanical, physical and thermal properties of granitic rocks—a review. International Journal of Rock Mechanics and Mining Sciences & Geomechanics Abstracts, 1983. Elsevier, 3-10.

ISRAEL METEOROLOGICAL SERVICE. 2017. *Israel Meteorological Service Data Base* [Online]. Israel Government Portal. [Accessed].

ITASCA CONSULTING GROUP INC. 2013a. 3DEC - Three-Dimensional Distinct Element Code, Ver. 5.0. Minneapolis: Itasca.

ITASCA CONSULTING GROUP INC. 2013b. 3DEC Manual. *User's Guide.* Minneapolis, Minesota.

ITASCA CONSULTING GROUP INC. 2013c. 3DEC Manual. *Theory and Background.* Minneapolis, Minesota.

ITASCA CONSULTING GROUP INC. 2013d. 3DEC Manual. *Optional Features.* Minneapolis, Minesota.

ITASCA, U. 1996. Universal distinct element code. *Users Manual,* 1.

IVERSON, R. M. 2000. Landslide triggering by rain infiltration. *Water Resources Research,* 36**,** 1897-1910.

JAEGER, J. C., COOK, N. G. & ZIMMERMAN, R. 2009. *Fundamentals of rock mechanics*, John Wiley & Sons.

JING, L. 2003. A review of techniques, advances and outstanding issues in numerical modelling for rock mechanics and rock engineering. *International Journal of Rock Mechanics and Mining Sciences,* 40**,** 283-353.

MATSUOKA, N. 2008. Frost weathering and rockwall erosion in the southeastern Swiss Alps: Long-term (1994–2006) observations. *Geomorphology,* 99**,** 353-368.

NAESER, N. D., NAESER, C. W. & MCCULLOH, T. H. 1989. The application of fission-track dating to the depositional and thermal history of rocks in sedimentary basins. *Thermal history of sedimentary basins.* Springer.

PASTEN, C. 2013. *Geomaterials Subjected To Repetitive Loading: Implications On Energy Systems.* Ph.D, Georgia Institute of Technology.

PASTEN, C., GARCíA, M. & CORTES, D. 2015a. Physical and numerical modelling of the thermally induced wedging mechanism. *Geotechnique Letters,* 5**,** 186-190.

PASTEN, C., GARCIA, M. & SANTAMARINA, C. 2015b. Thermo-mechanical ratcheting in jointed rock masses. *Géotechnique Letters*.

RODRIGUEZ, C. E., BOMMER, J. J. & CHANDLER, R. J. 1999. Earthquake-induced landslides: 1980-1997. *Soil Dynamics and Earthquake Engineering,* 18**,** 325-346.

ROHSENOW, W. M., HARTNETT, J. P. & CHO, Y. I. 1998. *Handbook of heat transfer*, McGraw-Hill New York.

SCHüTZ, F., NORDEN, B. & FöRSTER, D. G. 2012. Thermal properties of sediments in southern Israel: a comprehensive data set for heat flow and geothermal energy studies. *Basin Research,* 24**,** 357-376.

SHAPIRA, A., HOFSTETTER, R., ABDALLAH, A.-Q. F., DABBEEK, J. & HAYS, W. 2007. Earthquake hazard assessments for building codes. *Institutions,* 3**,** 8.

SHI, G.-H. 1993. *Block system modeling by discontinuous deformation analysis*, Computational mechanics.

TABOADA, A., GINOUVEZ, H., RENOUF, M. & AZEMARD, P. Landsliding generated by thermomechanical interactions between rock columns and wedging blocks: Study case from the Larzac Plateau (Southern France). EPJ Web of Conferences, 2017. EDP Sciences, 14012.

THE GEOPHYSICAL INSTITUTE OF ISRAEL. 2017. *Earthquakes In Israel* [Online]. http://www.gii.co.il/. [Accessed].

TURCOTTE, D. L. & SCHUBERT, G. 2014. *Geodynamics*, Cambridge University Press.

VáSáRHELYI, B. 2003. Some observations regarding the strength and deformability of sandstones in dry and saturated conditions. *Bulletin of Engineering Geology and the Environment,* 62**,** 245-249.

VUTUKURI, V., LAMA, R. & SALUJA, S. 1974. Handbook on Mechanical Properties of Rocks: Testing Techniques and Results, vol. I. Series on Rock and Soil Mechanics vol. 2, No. 1. *Trans Tech Publications, Clausthal, Germany, ISBN 0-87849-010-8*.

Appendices

Appendix A – Sliding on an inclined slope, gravity only (.3ddat file, 3DEC)

```
new
mscale off
title
Sliding under gravity loading
def setup
      base = 3 ; length of base
      lb = 0.8    ; sliding block length
      h = 0.6 ; sliding block height
      alpha = 25.0 ; sliding plane inclination
      alpha2 = 90-alpha ; cutting plane for sliding block sides
      def_right = 0.2 ; move the sliding block from the edge
      y1 = -0.25 ; model width
      y2 = 0.75
      x1 = def_right ; x value of lower left corner of sliding block
      z1 = (base-def_right) * tan(degrad*alpha) ; z coordinate of
lower left corner of sliding block
      x2 = x1 + lb*cos(degrad*alpha) ; x coordinate of lower right
corner of sliding block
      z2 = z1 - lb*sin(degrad*alpha) ; z coordinate of lower right
corner of sliding block
      x3 = x2 + h*sin(degrad*alpha) ; x coordinate of upper right
corner of sliding block
      z3 = z2 + h*cos(degrad*alpha) ; z coordinate of upper right
corner of sliding block
      ; Mechanical properties
      E = 24.486e9 ; Young's modulus
      nu = 0.2513 ; Poisson's ratio
      K = E/(3*(1-2*nu)) ; Bulk modulus
      G = E/(2*(1+nu)) ; Shear modulus
      Ks = 0.5e9 ; Shear stiffness of the joint
      Kn = 5e9 ; normal stiffness of the joint
      rho = 2140. ; density
      phi = 20. ; friction angle of the joint, change here for
different simulation
end
@setup
poly br 0 3 @y1 @y2 0 2
jset dip @alpha dd 90 or @x1 0 @z1 id 1 ; cut sliding plane
hide dip @alpha dd 90 or @x1 0 @z1 above
group block 'Sliding surface'
seek
hide dip @alpha dd 90 or @x1 0 @z1 below
jset dip @alpha2 dd -90 or @x1 0 @z1 ; cut back of sliding block
(left side of the sliding block)
delete dip @alpha2 dd -90 or @x1 0 @z1 above
jset dip @alpha2 dd -90 or @x2 0 @z2 ; cut right side of sliding
block
delete dip @alpha2 dd -90 or @x2 0 @z2 below
jset dip @alpha dd 90 or @x3 0 @z3 ; cut upper boundary of sliding
block
delete dip @alpha dd 90 or @x3 0 @z3 above
```

```
jset dip 90 dd 0 or 0 0 0 ; to avoid boundary problems, the sliding
block is in the middle of the sliding surface
delete dip 90 dd 0 or 0 0 0 below
jset dip 90 dd 0 or 0 0.5 0
delete dip 90 dd 0 or 0 0.5 0 above
group block 'Sliding block'
seek
plot create plot 'Model'
pl bl colorby group

; ------------- Zoning for deformable blocks -------------
;gen edge 0.080 ; One can verify also for deformable blocks

; ------------- Mechanical properties --------------------
prop mat 1 k @K g @G de @rho ; intact rock properties
prop jmat 1 jkn @Kn jks @ks jfric @phi ; joint properties

; ------------- Boundary conditions ----------------------
fix range group 'Sliding surface'
grav 0 0 -9.81

; ------------- Stepping to initial equilibrium ----------
hist id 1 unbal

damp local
solve ela only
damp 0,0

; ------------- Histories for solution --------------------

reset h ; reset all histories
reset d ; reset previous displacements
reset jd ; reset previous joint displacements
reset t ; reset time
reset v ; reset velocity
set time 0
hist id 1 time
hist id 2 sd @x2 0.25 @z2 dip @alpha dd 90 ; dip direction
displacement of the sliding block

; ------------- Solution ---------------------------------
plot create plot 'Shear disp'
plot hist 2 vs 1
solve time 1.

ret
```

Appendix B – Conduction in a plane sheet, after _ENREF_13_ENREF_24**ITASCA Consulting Group Inc. (2013d)**

```
new
; ------------------------------------------------------------
; conduction in a plane sheet
; explicit solution
; ------------------------------------------------------------
config thermal
;
title
Thermal conduction in a plane sheet - explicit solution
;
poly reg 0 0.8  0 0.5  0 0.6
plot create plot 'Blocks'
plot block
plot reset
;
prop mat 1 dens 2140.0
prop mat 1 k 1.6409e10 g 9784224407
prop jmat 1 jkn 5e9 jks 0.5e9
;
prop mat 1 cond 1.422458  spec_heat 850
prop mat 1 thexp 3.16e-6
;
gen edge 0.040
;
apply thermal temp 30. range x -0.01 0.01
apply thermal temp 0 range x 0.79 0.81
;
hist thtime
hist temp 0 0 0
hist temp 0 0 0.4
hist temp 0 0 0.8
;
set mech off
set thermal on
;
; --- fish constants ---
def cons
   c_cond = 1.422458         ; conductivity
   c_dens = 2140.            ; density
   c_sph = 850.              ; specific heat
   length = 0.8              ; wall thickness
   t1 = 30.                 ; wall temperature, face 1
   tabn = -1
   tabe = 0
   overl = 1. / length
   d = c_cond / (c_dens * c_sph)
   dol2 = d * overl * overl
   top = 2. / pi
   pi2 = pi * pi
```

```
    n_max = 100                ; max number of terms -exact solution
    teps = 1.e-5               ; small value compared to 1
end
def num_sol
    tabn = tabn + 2
    t_hat = thtime * dol2
    tp2 = t_hat * pi2
  ib_ = block_head
  loop while ib_ # 0
    gp_ = b_gp(ib_)
    loop while gp_ # 0
      rad = sqrt(gp_z(gp_)^2 + gp_y(gp_)^2) * overl
      if rad < 1.e-4 then
         z = gp_x(gp_) * overl
         table(tabn,z) = gp_temp(gp_) / t1
      end_if
      gp_ = gp_next(gp_)
    end_loop
    ib_ = b_next(ib_)
  end_loop
end
def ana_sol
    tabe = tabe + 2
    t_hat = thtime * dol2
    tp2 = t_hat * pi2
  ib_ = block_head
  loop while ib_ # 0
    gp_ = b_gp(ib_)
    loop while gp_ # 0
      rad = sqrt(gp_z(gp_)^2 + gp_y(gp_)^2) * overl
      if rad < 1.e-4 then
         z = gp_x(gp_) * overl
         n = 0
         nit = 0
         tsum = 0.0
         tsumo = 0.0
         converge = 0
         loop while n < n_max
            n = n + 1
            fn = float(n)
            term = sin(pi*z*fn) * exp(-tp2*fn*fn) / fn
            tsum = tsumo + term
            dddd = abs(term)
            if dddd < 1.0e-20 then
               nit = n
               table(tabe,z) = 1. - z - top * tsum
               converge = 1
               n = n_max
            else
               tsumo = tsum
            end_if
         end_loop
         if converge = 0 then
```

```
ii = out(' not converged: z= ' + string(z) + ' t = ' +
string(thtime))
            exit
         end_if
       end_if
       gp_ = gp_next(gp_)
     end_loop
     ib_ = b_next(ib_)
   end_loop
end
;
; --- settings ---
set mech off
set thermal on
; --- test ---
solve thtime 1e4
@cons
@num_sol
@ana_sol
solve thtime 5e4
@num_sol
@ana_sol
solve thtime 10e4
@num_sol
@ana_sol
;
table 1 name '3DEC 10,000 sec'
table 3 name '3DEC 50,000 sec'
table 5 name '3DEC 100,000  sec'
table 2 name 'Analytical 10,000 sec'
table 4 name 'Analytical 50,000 sec'
table 6 name 'Analytical 100,000  sec'
plot create plot 'Table'
pl table 1 style mark marks size 4 2 &
      3 style mark marks size 4 4 line style dash &
      5 style mark marks size 4 6 line style dot  &
      xaxis label 'X/L' yaxis label 'T/T0'
ret
```

Appendix C – Laboratory experiment simulation code (.3ddat file)

```
new
title
Lab experiment validation
config thermal
;
call model_geometry.3dfis ; import model geometry
plot create plot 'Lab model' ; plot physical model
pl bl colorby group color red blue yellow green
;
; ------------- Zoning for deformable blocks -------------
gen edge 0.040
;
; ------------- Mechanical properties --------------------
prop mat 1 k @K g @G dens @rho ; mechanical properties
prop mat 1 thexp @txp cond @cond spec @Cp ; thermal properties
prop jmat 1 jkn @Kn jks @Ks jfric @phi ; joints properties
;
; ------------- Boundary conditions ----------------------
bound nvel 0 range plane dip @alpha dd 90 or 0 0 @c1 dis 0.01 ;fix
displacement in the bottom
bound nvel 0 range plane dip @alpha dd 90 or 0 0 @c1 dis 0.01 ;fix
displacement in the bottom

      ;(twice for fix displacement in all directions)
bound nvel 0 range plane dip @alpha2 dd -90 or 0 0 @c1 dis 0.01 ;fix
normal displacement in the left side
grav 0 0 -9.81
ini temp 34.9 ; initial temperature
;
; ------------- Stepping to initial equilibrium ----------
set thermal off mech on
hist unbal
hist zdisp @c4x, 0, @c4z ; vertical displacement of upper right
corner of the sliding block
cyc 30000
;
; ------------- Histories for solution -------------------
set thermal on mech on
set th_time 0
set time 0
reset disp
reset jdisplacement
reset hist
hist unbal
hist thtime
hist sdisp @c4x 0 @c4z ; Shear displacement along the joint
hist zdisp 0.489858 0 0.734281 ; vertical displacement of the wedge
hist temp @c4x 0.25 @c4z ; applied temp
;
; ------------- Apply temperature history ----------------------
table 1 read 'tempHist_20_9.tab' ; temperature history of the
experiment (DataLogger)
```

```
apply thermal temp 1.0 hist table 1 range y -0.001 0.001 ; apply to
all faces of the model
apply thermal temp 1.0 hist table 1 range y 0.499 0.501
apply thermal temp 1.0 hist table 1 range plane dip @alpha dd 90 ori
0 0 @c1 dis 0.001
apply thermal temp 1.0 hist table 1 range plane dip @alpha2 dd -90
ori 0 0 @c1 dis 0.001
apply thermal temp 1.0 hist table 1 range plane dip @alpha2 dd -90
ori @c4x 0 @c4z dis 0.001
apply thermal temp 1.0 hist table 1 range plane dip @alpha dd 90 ori
@c5x 0 @c5z dis 0.001
;
; ------------- Solution ----------------------------------
solve thtime 1930200 force 0 ratio 0
plot create plot 'Sliding block displacement'
pl hist 3 vs 2 xaxis label 'Time (seconds)' yaxis label 'Dip
direction displacement (m)'
ret
```

Appendix D – Lab model geometry (.3dfis file)

```
title
Lab model generation
def setup
      ; mechanical properties
      phi = 21.28 ; friction angle
      rho = 2140. ; density
      E = 2.4486e10 ; Young's modulus
      nu = 0.2513 ; Poisson's ratio
      K = E/(3*(1-2*nu)) ; bulk modulus
      G = E/(2*(1+nu)) ; Shear modulus
      Ks = 0.5e9 ; shear stiffness
      Kn = 10*Ks ; normal stiffness
      ; thermal properties
      Cp = 850. ; specific heat capacity
      DT = 7.82e-7 ; thermal diffusivity
      cond = DT*rho*Cp ; thermal conductivity
      txp = 3.16e-6 ; thermal expansion coefficient
      ;  model geometry
      base = 1.5
      alpha = 15. ; slope inclination
      alpha2 = 90-alpha
      alpha3 = 90+alpha-20.14 ; wedge angle
      c1 = base*sin(degrad*alpha)
      c2 = base*cos(degrad*alpha)
      c3x = c2+0.2*sin(degrad*alpha)
      c3z = 0.2*cos(degrad*alpha)
      c4x = 0.8*sin(degrad*alpha)+1.22*cos(degrad*alpha)
      c4z = base*sin(degrad*alpha)+0.8*cos(degrad*alpha)-
1.22*sin(degrad*alpha)
      c5x = 0.8*sin(degrad*alpha)+0.42*cos(degrad*alpha)
      c5z = base*sin(degrad*alpha)+0.8*cos(degrad*alpha)-
0.42*sin(degrad*alpha)
      c6x = 0.8*sin(degrad*alpha)+0.2*cos(degrad*alpha)
      c6z = base*sin(degrad*alpha)+0.8*cos(degrad*alpha)-
0.2*sin(degrad*alpha)
      c7x =
0.42*cos(degrad*alpha)+0.2*sin(degrad*alpha)+0.05*sin(degrad*alpha)
      c7z = c3z+(1.5-0.42)*sin(degrad*alpha)+0.05*cos(degrad*alpha)
      command
            poly reg 0 2 0 0.5 0 2
            jset dip @alpha2 dd -90 or @c2 0 0 ; right side of
sliding surface
            delete range x @c2 3
            jset dip @alpha dd 90 or 0 0 @c1 ;bottom of sliding
surface
            delete dip @alpha dd 90 or 0 0 @c1 below
            jset dip @alpha2 dd -90 or 0 0 @c1 ; left side of the
model
            delete dip @alpha2 dd -90 or 0 0 @c1 above
            jset dip @alpha dd 90 or @c3x 0 @c3z ;top of sliding
surface
```

```
            jset dip @alpha dd 90 or @c4x 0 @c4z ; upper boundary of
the model
            delete dip @alpha dd 90 or @c4x 0 @c4z above
            hide dip @alpha dd 90 or @c3x 0 @c3z below
            jset dip @alpha2 dd -90 or @c4x 0 @c4z ; right side of
the sliding block
            delete dip @alpha2 dd -90 or @c4x 0 @c4z below
            jset dip @alpha2 dd -90 or @c5x 0 @c5z ; left joint of
the sliding block
            hide dip @alpha2 dd -90 or @c5x 0 @c5z below
            jset dip @alpha3 dd 90 or @c6x 0 @c6z ; left joint of the
wedge
            hide dip @alpha3 dd 90 or @c6x 0 @c6z below
            group block 'Wedge'
            hide
            seek dip @alpha dd 90 or @c3x 0 @c3z above
            hide dip @alpha2 dd -90 or @c5x 0 @c5z above
            group block 'Sliding block'
            seek
            hide range group 'Sliding block'
            hide range group 'Wedge'
            hide dip @alpha dd 90 or @c3x 0 @c3z below
            group block 'Rock mass'
            hide dip @alpha dd 90 or @c3x 0 @c3z above
            seek dip @alpha dd 90 or @c3x 0 @c3z below
            group block 'Sliding plane'
            hide
            seek range group 'Wedge'
            jset dip @alpha dd 90 or @c7x 0 @c7z  ; truncate wedge
            delete dip @alpha dd 90 or @c7x 0 @c7z below
            seek
      end_command
end
@setup
```

Appendix E – Block 1 Masada simulation (.3ddat file)

```
new
config thermal
call block1_new.3dfis
;
; ------------- Zoning for deformable blocks ------------
gen edge 0.3
;
; ------------- Mechanical properties --------------------
prop mat 1 k @K g @G dens @rho
prop mat 1 thexp @txp cond @lambda spec @Cp
prop jmat 1 jkn @Kn jks @Ks jfric @phi_peak
;
; ------------- Boundary conditions ----------------------
fix range group 'Rock mass'
grav 0 0 -9.81
ini temp 27.3 ; initial temperature
;
; ------------- Stepping to initial equilibrium ----------
set thermal off mech on ; switched thermal off for this step
hist id 1 unbal
hist id 2 zdisp @v8x @v8y @v8z ; vertical displacement of upper
right corner of the sliding block
hist id 3 zdisp 3.7 7.7 10.5 ; wedge vertical displacement, next to
v1
cyc 50000
plot create plot 'Equilibriate'
plot hist 1 ; plot unbalanced force vs step
;
; ------------- Histories for solution -------------------
set thermal on mech on
set th_time 0
set th_time 0
reset disp
reset jdisplacement
reset hist
hist id 1 thtime
hist id 2 temp @v8x @v8y @v8z ; applied temperature
hist id 3 sdisp @v4x @v4y @v4z ; Shear displacement of the sliding
block
hist id 4 sdisp 3.05 9.9 18.99 ; wedge displacement down the opening
joint
;
; ------------- Temperature history ----------------------
table 1 read ein_gedi_5yr.tab
apply thermal temp 1.0 hist table 1 range plane dip 0. dd 0. ori 0 0
@max_z distance 0.1 ; apply temp on top of the block
apply thermal temp 1.0 hist table 1 range plane dip @f1_dip dd
@f1_dd ori @v8x @v8y @v8z distance 0.1 ; face1
apply thermal temp 1.0 hist table 1 range plane dip @f2_dip dd
@f2_dd ori @v8x @v8y @v8z distance 0.1 ; face2
;
; ------------- Solution ---------------------------------
```

```
plot create plot 'Block 1 displacement'
plot hist 3 vs 1
plot create plot 'Wedge displacement'
plot hist 4 vs 1
;
set thdt 200 ; set time step to 200 seconds
solve thtime 157842000 force 0 ratio 0
```

Appendix F – Block 1 Masada geometry (.3ddis file)

```
title
Block 1 Masada geometry
def setup
      ; --- list of vetex of "Block 1" from SBL ---
      v1x = 4.55156100000000
      v1y = 8.21467800000000
      v1z = 4.49271900000000
      v2x = 6.18025400000000
      v2y = 13.7718220000000
      v2z = 5.13231200000000
      v3x = 8.32383600000000
      v3y = 4.23436200000000
      v3z = 2.54434200000000
      v4x = 10.3756750000000
      v4y = 7.05847500000000
      v4z = 2.50000000000000
      v5x = 2.
      v5y = 5.12143800000000
      v5z = 19.1038700000000
      v6x = 4.58926800000000
      v6y = 13.5905520000000
      v6z = 19.1038700000000
      v7x = 5.61066300000000
      v7y = 0.500000000000000
      v7z = 19.1038700000000
      v8x = 9.25283400000000
      v8y = 5.51301800000000
      v8z = 19.1038700000000
      min_x = 2.
      max_x = 10.3756750000000
      min_y = 2.
      max_y = 15.2718220000000
      min_z = 2.5
      max_z = 19.1038700000000
      ; --- f2 ---
      f2_dip = 90.
      f2_dd = 126.
      ; --- J1 ---
      j1_dip = 20.
      j1_dd = 124.
      ; --- J2 ---
      j2_dip = 84.
      j2_dd = 107.
      ; --- J3 ---
      j3_dip = 75.
      j3_dd = 52.
      ; --- f1 ---
      f1_dip = 84.
      f1_dd = 60.
      ; --- gap between block 1 and rock mass ---
      gap = -0.4
      v9x = v5x + gap*(cos(degrad*10.5)/sin(degrad*62.5))
```

```
      v9y = v5y + gap*(sin(degrad*10.5)/sin(degrad*62.5))
      v9z = v5z

      ; --- thermo-mechanical properties (from Bakun-Mazor et al.,
2013)---
      E = 40e9 ; Elastic modulus, Pa
      nu = 0.2 ; Poisson's ratio
      K = E/(3*(1-2*nu)) ; Bulk modulus, Pa
      G = E/(2*(1+nu)) ; Shear modulus, Pa
      rho = 2600. ; Density, kg/m^3
      phi_peak = 41. ; Peak friction angle, degrees
      phi_res = 23. ; Residual friction angle, degrees (from Hatzor
et al., 2004)
      Ks = 1e9 ; Shear stiffness, Pa/m
      Kn = 5e9 ; Normal stiffness, Pa/m (NOT in the paper)
      txp = 6e-6 ; Themal expansion coefficient, 1/C (6-8)
      lambda = 1.7 ; Thermal conductivity, W/m/k
      Cp = 810. ; Specific heat capacity, J/kg/k (Rohsenow et al.,
1998)

end
@setup
poly br 0 11 0 14.5 0 @max_z
; --- J1 (bedding plane) ---
jset id 11 dip @j1_dip dd @j1_dd or @v1x,@v1y,@v1z
hide dip @j1_dip dd @j1_dd or @v1x,@v1y,@v1z below
; --- J3 ---
jset id 33 dip @j3_dip dd @j3_dd or @v5x,@v5y,@v5z
hide dip @j3_dip dd @j3_dd or @v5x,@v5y,@v5z below
; --- J2 (block 1) ---
jset dip @j2_dip dd @j2_dd or @v5x,@v5y,@v5z ; cut block 1
jset id 22 dip 82.9 dd @j2_dd or @v9x,@v9y,@v9z ; making the gap
between the block 1 and the rock mass
hide
seek range x 4 4.5
group block 'Wedges'
seek blo 217
; --- f1 ---
jset dip @f1_dip dd @f1_dd or @v8x,@v8y,@v8z
delete dip @f1_dip dd @f1_dd or @v8x,@v8y,@v8z above
; --- f2 ---
jset dip @f2_dip dd @f2_dd or @v8x,@v8y,@v8z
delete dip @f2_dip dd @f2_dd or @v8x,@v8y,@v8z above
hide range group 'Wedges'
group block 'Block 1'
seek
hide range group 'Block 1'
hide range group 'Wedges'
join on
group block 'Rock mass'
seek
```

אוניברסיטת בן גוריון בנגב

הפקולטה למדעי הטבע

המחלקה למדעי הגיאולוגיה והסביבה

סימולציה נומרית של תנועת בלוק על מדרון עקב שינויי טמפרטורה

חיבור זה מהווה חלק מהדרישות לקבלת התואר "מוסמך למדעי הטבע" (M.Sc.)

מאת: יובל קיסר

בהנחיית: פרופ' יוסף חודרה חצור

ד"ר דגן בקון-מזור

אדר תשע"ח

מרץ 2018

אוניברסיטת בן גוריון בנגב

הפקולטה למדעי הטבע

המחלקה למדעי הגיאולוגיה והסביבה

סימולציה נומרית של תנועת בלוק על מדרון עקב שינויי טמפרטורה

חיבור זה מהווה חלק מהדרישות לקבלת התואר "מוסמך למדעי הטבע" (M.Sc.)

מאת: יובל קיסר

בהנחיית: פרופ' יוסף חודרה חצור

ד"ר דגן בקון-מזור

חתימת הסטודנט: _____ תאריך: _____

חתימת המנחה: _____ תאריך: __4.3.2018_____

חתימת המנחה: _____ תאריך: __4.3.2018_____

אדר תשע"ח

מרץ 2018

תקציר

במחקר זה נחקר מנגנון תרמו-מכני ליציבות מדרונות באמצעות גרסה תלת-מימדית של השיטה הנומרית Distinct Element Method (DEM). מטרתנו היא לבחון האם תנודות טמפרטורת פני השטח, היומיות או השנתיות, יכולות לגרום לתזוזה בלתי הפיכה וכשל במדרון סלעי, וליצור מודל כמותי המתאר תזוזה הנובעת משינויי הטמפרטורה. בעיות של הולכת חום הן לעתים קרובות מורכבות מדי לפתרון באמצעים אנליטיים בלבד. גישות נומריות מאפשרות לנו ללמוד בעיות גיאומכניות מורכבות, אשר אין להן פתרונות אנליטיים מדויקים. אנו בונים מודל תלת מימדי ב-3DEC כדי לדמות את ההתרחבות התרמית של הבלוק הגולש, ואת התזוזה הפלסטית במדרון חיבובי נטוי הנגרמת מכך. על פי המנגנון המוצע, ההנחה היא שתהליך זה הוא בלתי הפיך. התוצאות שלנו מראות כי תזוזה במורד מדרון אכן מתרחשת כאשר גבולות הבלוק חשופים לטמפרטורות משתנות. התוצאות של המודל הנומרי מושוות לתוצאות ניסויי מעבדה המתקבלות ממודל פיזי בחדר מבוקר אקלים (Feldheim, 2017).

אנו משווים סימולציות נומריות עם מדידות תזוזה של בלוק במדרון המזרחי של הר מצדה, שעד לאחרונה ההנחה הייתה שהמנגנון השולט בתזוזה הוא סייסמי. על ידי יישום הגישה הנומרית על הממדים הפיזיים המדויקים של הבלוק בשדה אנו מוצאים כי, למעשה, העמסה תרמית לבדה יכולה להסביר את התזוזה המצטברת שנמדדה בשדה.

אנו מאמינים שמנגנון הכשל התרמי החדש עשוי להיות גורם משמעותי בבעיות יציבות המדרון בשל האופי המצטבר והחוזר של התזוזה, במיוחד במדרונות במסת סלע סדוקה שנחשפים לתנודות טמפרטורה גבוהות.